UNIVERSIDADE DA BEIRA INTERIOR

Ciências da Saúde

# Andaimes bioativos produzidos por impressão 3D para aplicação na regeneração óssea

**Cátia Solange Duarte Cabral**

Dissertação para obtenção do Grau de Mestre em

**Ciências Biomédicas**

(2º ciclo de estudos)

Orientador: Professor Doutor Ilídio Joaquim Sobreira Correia

Co-orientador: Mestre Sónia Alexandra Pereira Miguel

**Covilhã, outubro de 2018**

*“Don’t worry about failures, worry about the chances you miss when you don’t even try.”*

***Jack Canfield***

*Aos meus pilares, pais e avós.*

# Agradecimentos

Em primeiro lugar, gostaria de agradecer ao meu orientador Professor Ilídio Correia, pela oportunidade que me concedeu em integrar este grupo de investigação e por sempre proporcionar as condições necessárias para ter conseguido desenvolver este trabalho. A sua exigência e orientação foram essenciais para o desenvolvimento desta tese. Agradeço também pelos conselhos e ensinamentos que me transmitiu ao longo deste ano e pela sua boa disposição, os quais me mostraram que um bom ambiente de trabalho e exigência se conseguem conciliar para alcançar o sucesso.

À minha co-orientadora, mestre Sónia Miguel, quero dedicar um especial agradecimento pela sua incansável ajuda, paciência e por todos os ensinamentos que me transmitiu. Obrigada pelos momentos descontraídos e, sobretudo, por aqueles em que foi preciso um 'abanão'. Não há forma suficiente de agradecer pelo apoio constante, pelo à vontade e confiança que depositou em mim. Obrigada por, sem dúvida, tornar esta caminhada mais fácil em todos os sentidos!

Aos meus colegas de grupo de investigação, gostaria de agradecer pelo seu apoio e ótimo ambiente de trabalho. Ao Duarte, pela sua constante troca de ideias, pela ajuda que me deu e por me transmitir que o rigor é a chave para um trabalho bem executado. À Elisabete, por sempre me dar o seu apoio, pelos conselhos e pela sua contagiante boa disposição. Ao André, que sempre deu o seu auxílio na parte tecnológica e me desafiou com a sua troca de conhecimentos. Gostaria também de agradecer à minha parceira de laboratório, Déborah, pelo apoio, ajuda e pelos momentos divertidos que vivemos durante esta jornada.

Um obrigado a todas as minhas colegas da 'salinha' pelas gargalhadas e ideias que partilhámos juntas. À Rita e à Sofia, pela amizade que se fortaleceu e pelas confidentes que se tornaram. À minha *sister* Carol e minha homónima Cátia, as quais me fizeram sempre encontrar o lado bom das coisas. À Catarina e à Raquel por constantemente colocarem uma risada em tudo o que dizem. Agradecer ainda à Rita A., que mesmo pertencendo a outro grupo de investigação, nunca descuidou da sua amizade e apoio. De todas vós levo sorrisos.

Às minhas meninas da Vila, obrigada por sempre estarem presentes e arranjarem um bocadinho dos seus dias para estarem comigo, mesmo com a minha constante falta de tempo. Obrigada por fazerem parte de todas as etapas da minha vida e por todos os dias vincularem o lema de que "qualquer amizade que ultrapassa a marca de sete anos é mais provável que dure uma vida inteira."

Aos mais importantes, os meus pais e avós. Não há forma de expressar a gratidão que sinto por todo o apoio que depositam em mim, pela compreensão nos momentos mais difíceis, pelo sacrifício e pelo amor incondicional. Um obrigado sobretudo pelos valores que continuamente me transmitem, ninguém no mundo o sabe fazer melhor do que vocês. À minha mãe, que é irmã e amiga agradeço pelos conselhos e por querer sempre fazer de mim uma pessoa melhor. Ao meu pai, pelo carinho mesmo nas suas poucas palavras, por todos os dias me mostrar que é possível aliar o sentido de responsabilidade à boa disposição. Aos meus eternos avós, por ser sempre a sua menina, não consigo agradecer o seu gigante amor.

Por fim, e nunca menos importante, um obrigado ao Alexandre, o meu melhor amigo e companheiro de viagem destes seis anos. Agradeço profundamente pelo cuidado e carinho, por me motivar a nunca parar de lutar, por sempre acreditar em mim e, sobretudo, por me fazer acreditar em mim mesma. Por todo o amor, obrigado!

A todos agradeço muito por fazerem parte desta caminhada. Levo comigo um pouco de cada um de vocês!

# Resumo

A incidência mundial de doenças que afetam o tecido ósseo tem apresentado um crescimento acentuado e prevê-se que este número duplique até 2020, especialmente em populações onde o envelhecimento está associado ao aumento da obesidade e à pouca atividade física. Nos dias de hoje, o tratamento deste tipo de patologias tem sido efetuado recorrendo ao uso de enxertos ósseos. Contudo, esta abordagem apresenta diversas limitações tais como disponibilidade do enxerto, possibilidade de induzir dor crónica no paciente e rejeição imunológica. Neste contexto, os investigadores da área de Engenharia de Tecidos têm desenvolvido estruturas 3D (andaimes) que reproduzam as propriedades mecânicas e biológicas do osso nativo e que possam ser usadas no processo de regeneração óssea. A produção de andaimes através de técnicas de prototipagem rápida tem permitido o desenvolvimento de estruturas com geometria e tamanho definidos e, ainda a combinação de diferentes tipos de materiais (cerâmicas/polímeros) de forma a mimetizar a matriz inorgânica/orgânica do osso nativo. Recentemente, com o intuito de reforçar as propriedades mecânicas e osteogénicas destas estruturas 3D, os investigadores procederam à incorporação de materiais derivados de grafeno, como o óxido de grafeno (GO) e o óxido de grafeno reduzido (rGO) na sua composição. O rGO tem recebido destaque para aplicação na regeneração óssea, devido à sua elevada força de compressão, bem como grande capacidade de adsorção de cálcio na sua superfície, em comparação com o GO. No entanto, o rGO apresenta reduzida estabilidade em soluções aquosas, o que dificulta a sua direta incorporação na mistura de cerâmica/polímero, que é usada na produção dos andaimes.

No presente estudo foram produzidos andaimes compostos por fosfato tricálcico, quitosano e gelatina (TGC) e óxido grafeno (TGC_GO), usando uma Fab@Home 3D-Plotter. Posteriormente, os andaimes foram funcionalizados com rGO, usando o método de redução *in situ*, e o ácido ascórbico como agente redutor, com o intuito de melhorar as propriedades mecânicas e biológicas dos andaimes. Os resultados obtidos revelaram que os andaimes TGC_irGO apresentaram melhores propriedades mecânicas, em comparação com as outras estruturas 3D produzidas. Além disso, os andaimes TGC_irGO mostraram uma melhor capacidade em adsorver cálcio na sua superfície, aumentando desta forma a atividade da fosfatase alcalina. Por outro lado, os andaimes produzidos apresentaram também atividade antimicrobiana, sem, no entanto, comprometerem a viabilidade e proliferação dos osteoblastos. Os resultados obtidos demonstraram que os andaimes produzidos com TGC_irGO possuem elevado potencial para serem aplicados na regeneração óssea.

# Palavras-chave

Andaimes; Óxido de Grafeno reduzido; Prototipagem Rápida; Regeneração óssea.

# Resumo alargado

O osso é um tecido extremamente dinâmico e vascularizado, que está envolvido na locomoção, suporte e ainda na proteção dos órgãos vitais contra ameaças externas e no armazenamento de minerais essenciais à homeostase do corpo humano. O tecido ósseo tem na sua composição matriz orgânica (maioritariamente colagénio tipo I), matriz inorgânica (hidroxiapatita), células (osteoblastos, osteócitos e osteoclastos) e água. Apesar deste tecido possuir capacidade de autorregeneração, esta não é suficiente para reparar defeitos críticos resultantes das fraturas ósseas associadas à idade avançada, doenças ou traumas. O envelhecimento tem sido identificado como uma das principais causas para o aumento da incidência mundial de desordens que afetam o tecido ósseo, a qual se prevê que duplique até 2020. Na atualidade, o tratamento das fraturas que afetam o tecido ósseo tem sido realizado através da utilização de autoenxertos, aloenxertos ou xenoenxertos. Contudo, a frequente ocorrência de infeções e o risco elevado de rejeição dos implantes podem comprometer a aplicação destas abordagens terapêuticas.

Neste contexto, os investigadores da área de Engenharia de Tecidos têm vindo a desenvolver estruturas 3D (andaimes) que sejam capazes de reproduzir as propriedades mecânicas e biológicas do osso nativo, assim como induzir o processo de regeneração óssea. Estas estruturas têm o propósito de atuar como suporte temporário para auxiliar o processo de formação do novo tecido ósseo. O sucesso destes andaimes está dependente de propriedades como biocompatibilidade, biodegradabilidade, porosidade, resistência mecânica, osteoinductividade e osteoconductividade. De entre os diversos tipos de andaimes já explorados pelos investigadores, os andaimes produzidos através de técnicas de prototipagem rápida apresentam propriedades que os destacam dos restantes, uma vez que estes métodos permitem obter andaimes com estruturas e geometrias definidas, possibilitando o desenvolvimento de estruturas a partir de dados do próprio paciente. Por outro lado, a escolha de materiais que proporcionem a produção de andaimes com propriedades requeridas é fundamental. Neste sentido, os investigadores têm usado vários materiais que incluem cerâmicas (hidroxiapatita), metais (titânio e cobalto), polímeros (quitosano, alginato e gelatina) e compósitos, de forma a mimetizar as fases inorgânicas/orgânicas que constituem o osso nativo.

Em estudos recentes, os investigadores têm incorporado materiais derivados de grafeno na estrutura dos andaimes, com o objetivo de reforçar as propriedades mecânicas e osteogénicas dos andaimes. O óxido de grafeno reduzido (rGO) possui uma elevada força de compressão e tem uma maior capacidade de adsorção de cálcio na sua superfície, em comparação com o óxido de grafeno (GO). No entanto, o rGO apresenta reduzida estabilidade em soluções aquosas, o que dificulta a sua incorporação na mistura de cerâmica/polímero usada na produção dos andaimes.

O presente estudo teve como principal objetivo o desenvolvimento de um novo processo de funcionalização de andaimes 3D com rGO. Para isso, os andaimes compostos por fosfato tricálcico, quitosano e gelatina (TGC) e óxido de grafeno (TGC_GO) foram produzidos usando uma Fab@Home 3D-Plotter. Posteriormente, as estruturas 3D produzidas foram funcionalizadas com rGO, usando o método de redução *in situ*, e o ácido ascórbico como agente redutor. A eficiência do método de produção foi caracterizada através da avaliação das propriedades dos andaimes produzidos com TGC_irGO, TGC (não funcionalizados) e os TGC_GO (contendo GO na sua composição). Os resultados obtidos revelam que os andaimes TGC_irGO apresentam melhores propriedades mecânicas, em comparação com os outros andaimes produzidos. Além disso, a funcionalização dos andaimes com rGO revelou um maior aumento de deposição de cálcio na sua superfície, aumentando também a atividade da fosfatase alcalina, durante os 21 dias de incubação. Por outro lado, a atividade antimicrobiana dos andaimes produzidos foi também avaliada usando *Staphylococcus aureus* e *Escherichia coli,* como bactérias-modelo. Os andaimes não induziram nenhum efeito tóxico nos osteoblastos, promovendo a adesão destas células na superfície dos andaimes, bem como a sua infiltração no seu interior.

Os resultados obtidos neste trabalho revelaram que os andaimes TGC_irGO apresentam propriedades promissoras que poderão potenciar a sua aplicação na regeneração óssea.

# Abstract

The incidence of bone disorders affecting the worldwide population has been presenting a steeply upward and it is expected to double by 2020, especially in populations where aging is associated with increased obesity and poor physical activity. The treatment of these types of disorders have been performed using bone grafts. However, these approaches have several limitations such as limited availability, induction of chronic pain to the patient as well as immune rejection. To surpass these limitations, researchers from Tissue Engineering area have been developing 3D structures, known as scaffolds, that are able to reproduce the mechanical and biological features of the native bone, as well as to promote the bone regenerative process. Among the techniques usually used for the production of these scaffolds, rapid prototyping techniques have been the most applied since they allow the production of structures with defined geometry and sizes. In addition, different types of materials (ceramics/polymers), have been selected to produce scaffolds that are able to mimic the inorganic/organic matrices of native bone. In order to improve the mechanical and osteogenic properties of the scaffolds, the researchers recently have incorporated graphene-derived materials into scaffolds structure. Reduced graphene oxide (rGO) possess great compressive strength and higher capacity to promote the calcium deposition at its surface, in comparison with graphene oxide (GO). However, rGO exhibits a lower stability in aqueous solutions, which impair its direct incorporation into ceramic/polymer mixture used for scaffolds production.

The present work aimed to develop new 3D scaffolds functionalized with rGO. To accomplish that, the scaffolds composed by tricalcium phosphate, chitosan and gelatin (TGC) and graphene oxide (TGC_GO) were produced using a Fab@Home 3D-Plotter. After that, the scaffolds were functionalized with rGO through *in situ* reduction process, using the L-Ascorbic acid as reducing agent, obtaining TGC_irGO scaffolds. The results obtained revealed that the TGC_irGO scaffolds present enhanced mechanical properties without compromising their porosity. Moreover, the TGC_irGO scaffolds display an improved calcium deposit at their surface and were able to increase the alkaline phosphatase (ALP) activity. In addition, scaffolds also inhibited the microorganism' growth, without compromising the viability and proliferation of osteoblasts. Such features reveal the potential of the TGC_irGO scaffolds for bone tissue regeneration applications as well as validate the protocol employed to functionalize the scaffolds.

# Keywords

3D scaffolds; Bone regeneration; Reduced graphene oxide; Rapid prototyping.

# Table of Contents

## Chapter I

1. Introduction ........ 2

  1.1. Bone Tissue ........ 2

  1.2. Bone Anatomy and Morphology ........ 2

  1.3. Bone Histology ........ 4

    1.3.1. Bone Matrix ........ 4

    1.3.2. Bone cells ........ 5

      1.3.2.1. Osteoblasts ........ 5

      1.3.2.2. Bone lining cells ........ 6

      1.3.2.3. Osteocytes ........ 6

      1.3.2.4. Osteoclasts ........ 6

  1.4. Bone regeneration process ........ 7

    1.4.1. Primary (direct) bone healing ........ 8

    1.4.2. Secondary (indirect) bone healing ........ 8

  1.5. Bone Disorders ........ 9

    1.5.1. Osteoporosis ........ 10

    1.5.2. Pagets' Disease ........ 10

    1.5.3. Osteomyelitis ........ 10

    1.5.4. Osteoarthritis ........ 10

  1.6. Bone Grafts ........ 11

  1.7. Tissue Engineering ........ 12

    1.7.1. Properties exhibited by 3D scaffolds aimed for bone regeneration ........ 12

1.7.1.1. Biocompatibility ........ 13
1.7.1.2. Biodegradability ........ 13
1.7.1.3. Surface properties, osteoconductivity and osteoinductivity ........ 13
1.7.1.4. Mechanical Properties ........ 14
1.7.1.5. Porosity ........ 14
1.7.1.6. Antibacterial activity ........ 14
1.7.2. Techniques used for scaffold fabrication ........ 15
1.7.2.1. Scaffold fabrication with a Fab@Home 3D Plotter ........ 15
1.7.3. Biomaterials used for scaffold fabrication ........ 16
1.7.3.1. Metals ........ 16
1.7.3.2. Ceramics ........ 16
1.7.3.3. Polymers ........ 17
1.7.3.3.1. Natural Polymers ........ 17
1.7.3.3.2. Synthetic Polymers ........ 19
1.7.3.4. Composites ........ 19
1.7.3.5. Graphene-based materials ........ 19
1.7.3.5.1. Graphene Oxide ........ 19
1.7.3.5.2. Reduced Graphene Oxide ........ 20
1.8. Aims ........ 22

## Chapter II

2. Materials and Methods ........ 24
2.1. Materials ........ 24
2.2. Methods ........ 24
2.2.1. Preparation and characterization of GO and rGO (direct reduction with LAA) ... 24

2.2.2. Production of TGC_irGO scaffolds ........ 25
2.2.3. Characterization of the morphology of the 3D scaffolds ........ 25
2.2.4. Characterization of the physico-chemical properties of the scaffolds ........ 26
2.2.4.1. ATR-FTIR and EDS analysis ........ 26
2.2.5. Characterization of the mechanical properties of the scaffolds ........ 26
2.2.6. Characterization of the swelling profile of the scaffolds ........ 27
2.2.7. Contact angle measurements ........ 27
2.2.8. Evaluation of scaffolds' porosity ........ 27
2.2.9. Analysis of the enzymatic biodegradation profile of the scaffolds ........ 28
2.2.10. *In vitro* biomineralization assay ........ 28
2.2.11. Characterization of the biological properties of the scaffolds ........ 28
2.2.11.1. Evaluation of cell viability and proliferation in contact with the scaffolds .. 28
2.2.11.2. Characterization of cell adhesion at the surface of the scaffolds ........ 29
2.2.11.3. Confocal microscopic analysis ........ 29
2.2.11.4. Alizarin Red S (ARS) staining ........ 29
2.2.11.5. Alkaline Phosphatase (ALP) activity and dsDNA quantification ........ 30
2.2.12. Evaluation of the bactericidal activity of the scaffolds ........ 30
2.2.13. Statistical analysis ........ 31

## Chapter III

3. Results and Discussion ........ 33
3.1. Characterization of GO and rGO produced by direct reduction with LAA ........ 33
3.2. Morphological characterization of the scaffolds ........ 34
3.3. Characterization of the physico-chemical properties of the produced scaffolds ....... 37
3.4. Characterization of the mechanical properties of the scaffolds ........ 38

3.5. Evaluation of the swelling profile of the produced scaffolds .............................. 39

3.6. Determination of the wettability of the surface of the produced 3D scaffolds ........ 39

3.7. Evaluation of scaffolds' porosity ............................................................... 40

3.8. Characterization of enzymatic degradation profile of the scaffolds ..................... 41

3.9. *In vitro* biomineralization assay ................................................................ 42

3.10. Characterization of the biological properties of the produced scaffolds .............. 43

3.10.1. Evaluation of scaffolds' cytotoxic profile............................................... 43

3.10.2. Confocal laser scanning microscopy (CLSM) analysis .................................. 46

3.10.3. Alizarin Red S (ARS) staining ............................................................. 48

3.10.4. Determination of the Alkaline Phosphatase (ALP) activity ........................... 48

3.11. Evaluation of the bactericidal activity of the scaffolds................................... 49

## Chapter IV

4. Conclusion and Future Perspectives .................................................. 52

## Chapter V

5. References ......................................................................................... 54

# List of Figures

Figure 1. Schematic representation of the internal structure and organization of the bone ....3

Figure 2. Schematic representation of the cells found in bone tissue ..............................5

Figure 3. Illustration of the typical fracture healing phases ..........................................7

Figure 4. Representation of the main disorders that affect the bone tissue .......................9

Figure 5. Representative illustration of the main strategies used in the BTE .................... 12

Figure 6. Chemical structure of tricalcium phosphate .............................................. 17

Figure 7. Chemical structure of gelatin................................................................ 18

Figure 8. Chemical structure of chitosan ............................................................... 18

Figure 9. Chemical structure of graphene oxide and reduced graphene oxide ................... 21

Figure 10. Schematic representation of the experimental setup used to produce TGC, TGC_GO and TGC_irGO scaffolds ................................................................... 22

Figure 11. Characterization of physico-chemical properties of GO and rGO...................... 33

Figure 12. Production and characterization of 3D scaffolds. Schematic representation of experimental setup used to produce the TGC_irGO scaffolds production ........... 36

Figure 13. ATR-FTIR analysis of TCP, Gel, CH (A); TGC, TGC_GO, TGC_irGO scaffolds (B) .... 37

Figure 14. Characterization of the $C_s$ (A) and YM (B) of the produced 3D scaffolds ............ 39

Figure 15. SEM images that characterize the pore diameters on scaffolds' surfaces ........... 41

Figure 16. Characterization of physico-chemical properties of the produced scaffolds ........ 42

Figure 17. Evaluation of the biomineralization at the surface of the produced scaffolds in contact with SBF ......................................................................... 43

Figure 18. Optical microscopy images acquired to characterize cells' behaviour in contact with the produced scaffolds during 1, 3 and 7 days ........................................... 45

Figure 19. Characterization of the biological properties of the scaffolds ......................... 46

Figure 20. CLSM images acquired to characterize cell internalization within the TGC, TGC_GO and TGC_irGO scaffolds ..... 47

Figure 21. Characterization of the osteogenic properties of the produced scaffolds ..... 49

Figure 22. Characterization of the antimicrobial activity of the produced scaffolds ..... 50

# List of Tables

Table 1. EDS analysis of GO and rGO produced by direct reduction of GO with LAA ........... 34

Table 2. EDS analysis of the 3D printed scaffolds ..................................................... 38

# Acronyms

| | |
|---|---|
| AA | Acetic Acid |
| ALP | Alkaline Phosphatase |
| ARS | Alizarin Red S |
| ATR-FTIR | Attenuated Total Reflectance-Fourier Transformed Infrared Spectroscopy |
| BLC | Bone Lining Cells |
| BMP | Bone Morphogenic Proteins |
| BTE | Bone Tissue Engineering |
| $Ca^{2+}$ | Calcium |
| CAD | Computer Assisted Design |
| CAM | Computer-Aided Manufacturing |
| CH | Chitosan |
| CS | Compressive Strength |
| CSLM | Confocal Selective Laser Microscopy |
| DLS | Dynamic Light Scattering |
| DMEM-F12 | Dulbecco's Modified Eagle's Medium: Nutrient Mixture F-12 |
| ECM | Extracellular Matrix |
| EDS | Energy Dispersive Spectroscopy |
| EDTA | Ethylenediamine Tetraacetic Acid |
| EtOH | Ethanol |
| FBS | Fetal Bovine Serum |
| Gel | Gelatin |
| GO | Graphene Oxide |
| HA | Hydroxyapatite |
| HCl | Hydrochloric Acid |
| hOB | Human Osteoblasts |
| IGF | Insulin-Like Growth Factor |
| IL-1 | Interleukin-1 |
| IL-6 | Interleukin-6 |
| irGO | *In Situ* Reduction of GO |
| LAA | L-Ascorbic Acid |
| M-CSF | Macrophage Colony-Stimulating Factor |
| MHC | Major Histocompatibility Complex |
| MSC | Mesenchymal Stem Cell |
| MTS | 3-(4,5-dimethylthiazol-2-yl)-5-(3-carboxymethoxyphenyl)-2-(4-sulfophenyl)-2H tetrazolium salt |
| NaOH | Sodium Hydroxide |

| | |
|---|---|
| NCP | Noncollagenous Protein |
| $PO_4^{3-}$ | Phosphate |
| PBS | Phosphate Buffered Saline |
| PCL | Polycaprolactone |
| PFA | Paraformaldehyde |
| PGA | Polyglycolic Acid |
| PI | Propidium Iodide |
| PLA | Polylactic Acid |
| PLGA | Poly(lactic-co-glycolic) Acid |
| pNPP | *p*-Nitrophenylphosphate |
| PT | Parathyroid Hormone |
| RANKL | Receptor Activator of Nuclear Factor Kappa-ß Ligand |
| RGD | Arginine-Glycine-Aspartic Acid |
| rGO | Reduced Graphene Oxide |
| RP | Rapid Prototyping |
| RT | Room Temperature |
| SBF | Simulated Body Fluid |
| SEM | Scanning Electron Microscopy |
| TE | Tissue Engineering |
| Ti | Titanium |
| TGC | Tricalcium Phosphate/Gelatin/Chitosan |
| TGC_GO | Tricalcium Phosphate/Gelatin/Chitosan/Graphene oxide |
| TGC_irGO | Tricalcium Phosphate/Gelatin/Chitosan/*In situ* Reduced Graphene Oxide |
| TGF-ß | Transforming Growth Factor |
| TNF-α | Tumor Necrosis Factor-α |
| TPP | Tripolyphosphate |
| UV | Ultraviolet |
| WCA | Water Contact Angle |
| YM | Young Modulus |

# Chapter I

# 1. Introduction

## 1.1. Bone Tissue

Bone is a complex, specialized and highly dynamic tissue, that plays critical roles in human physiology [1, 2]. Bone tissue provides structural support to the body, allow locomotion, as well as protect vital internal organs from hazard agents [3, 4]. Moreover, it is also involved in the maintenance of mineral homeostasis, acts as reservoir of growth factors and essential minerals, like calcium and phosphorous, as wells as provide suitable environment for hematopoiesis [5, 6]. As a dynamic tissue, bones are under constant remodelling and exhibit self-healing capacity, i.e. they can regenerate by themselves from non-critical lesions [7, 8].

In terms of composition, bone tissue is comprised of cells (osteoblasts, bone lining cells, osteocytes, and osteoclasts), water, bone matrix and blood vessels. Bone cells are embedded in the bone extracellular matrix (ECM), which is composed of an organic (35%) and an inorganic (65%) component [9]. The organic phase is mainly composed by ECM proteins (e.g. collagen, osteopontin, osteonectin, osteocalcin, thrombospondin, tenascin, fibronectin, laminin, glycosaminoglycans and proteoglycans) which provides flexibility and elasticity, whereas its inorganic phase contains calcium phosphate crystals, namely hydroxyapatite (HA), granting the required mechanical properties to the bone, i.e., stiffness and resistance to compression. In turn, the blood vessels regulate blood supply as wells as bone remodelling [10, 11].

## 1.2. Bone Anatomy and Morphology

The adult human skeleton is constituted by a total of 213 bones, excluding the sesamoid bones, which can be categorized according to their shape, morphology and bone matrix [12]. Bone tissue, depending on its shape, is classified as long, short, flat or irregular [1].

Long bones include the clavicles, humerus, radius, femur and tibiae. These bones display a cylindrical shape and a great mechanical strength. Long bones (Figure 1) are composed of a diaphysis (hollow shaft), cone-shaped metaphyses below the growth plates, and rounded epiphyses above the growth plates. The diaphysis is composed primarily of bulk bone with a cortical periphery and cancellous interior, whereas the metaphysis and epiphysis are formed by trabecular meshwork bone surrounded by a relatively thin shell of dense cortical bone [12].

At morphological level, bone tissue is classified as cortical (or compact) and trabecular (or cancellous), according to the density of the bone matrix [6]. Cortical bone is dense, solid and surrounds the marrow space, having a small number of cells and blood vessels [1, 6, 13]. It is composed by cortical osteons, also called Haversian systems. Haversian systems present a cylindrical shape and provide a central canal that is responsible for the transport of nutrients. The walls of Haversian systems are formed by a concentric lamellae, which provide its mechanical resilience [6, 13]. Cortical bone has an outer periosteal and inner endosteal surface. The outer surface of the cortical bone is covered by the periosteum, a fibrous connective tissue sheath composed by two layers. The outer layer is composed by a fibrous collagenous tissue (Sharpeys' fibers), with blood vessels and nerves, whereas the inner layer is formed by a layer of bone cells [12, 14, 15].

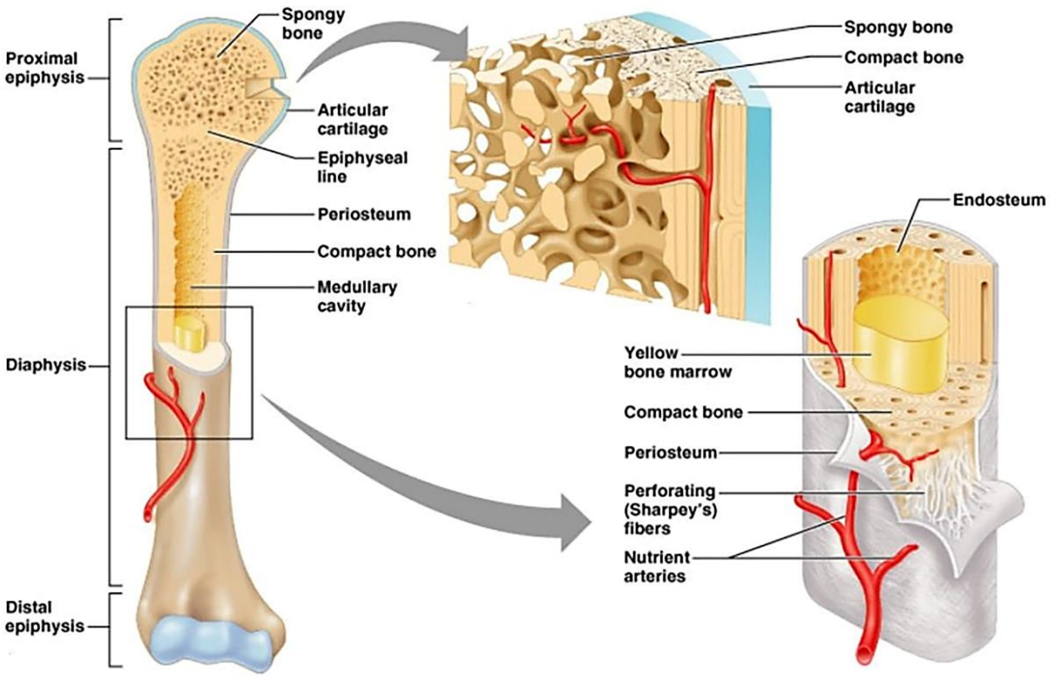
Proximal epiphysis
Diaphysis
Distal epiphysis
Spongy bone
Articular cartilage
Epiphyseal line
Periosteum
Compact bone
Medullary cavity
Spongy bone
Compact bone
Articular cartilage
Endosteum
Yellow bone marrow
Compact bone
Periosteum
Perforating (Sharpey's) fibers
Nutrient arteries

**Figure 1.** Schematic representation of the internal structure and organization of the bone (adapted from [16]).

On the other side, the trabecular bone presents a high porosity (50-90%) and has a compressive strength almost 20 times lower in comparison to the cortical bone [15, 17]. Its interconnected porous structure is filled with bone marrow that favours the metabolic activities, like the nutrients and gases diffusion as well as the removal of metabolic waste residues [6, 18]. Additionally, the cancellous bone is arranged in a sponge-like form, with a honeycomb of branching plates and rods, known as trabeculae [19, 20]. The trabeculae are lined with another connective tissue membrane (endosteum), that is composed by a single layer of cells [12].

The cortical bone is found in diaphysis of the long bones, whereas cancellous bone is present in interior of the flat, short and irregular bones [12, 21]. Furthermore, cortical and trabecular bone are normally arranged in a lamellar pattern, in which collagen fibrils are laid down with alternating orientations. The mechanism by which osteoblasts lay down collagen fibrils in a lamellar pattern is unknown, but lamellar bone displays significant strength, as a result of the orientation of the collagen fibrils [22]. In opposition, in the woven bone the collagen fibrils are disorganized, leading to a weaker mechanical strength. Woven bone is usually produced during the production of primary bone and may also be seen in high bone turnover states such as osteitis fibrosa cystica or in Paget's disease [6, 9, 23].

The adult human skeleton is composed of 80% cortical and 20% trabecular bone. However, depending on the bones and skeletal sites, the ratios of cortical to trabecular bone are different. For example, the vertebra presents a ratio of 25:75 of cortical to trabecular bone. Such ratio is 50:50 in the femoral head and 95:5 in the radial diaphysis [12]. The architectural differences found between cortical and trabecular bone are responsible for their different mechanical properties [9].

## 1.3. Bone Histology

### 1.3.1. Bone Matrix

The ECM of bone is composed of organic and inorganic components, in a ratio of 35%/65%, that can vary depending on the age of the individual [24-26]. The organic phase is mainly constituted by collagen type I, trace amounts of collagen types III and V in certain stages of bone formation. Moreover, noncollagenous proteins (NCP), which constitute 10-15% of total bone protein content can be divided into structural proteins and promoters of biological processes [26, 27]. The first group of proteins (such as fibronectin, osteocalcin, osteopontin, osteonectin, bone sialoprotein II, decorin and biglycan) play a structural and mechanical role [4, 28]. On the other side, the second group contains proteins (transforming growth factors-ß (TGF- ß1, TGF- ß2 and TGF-ß3), insulin-like growth factors (IGFs), and bone morphogenic protein (BMPs)) that modulate the function of bone cells through the interaction with their cell-surface receptors, proteases, hormones and other biomolecules [13, 29].

In turn, the inorganic phase of bone matrix is mainly composed of crystalline mineral salts in the form of hydroxyapatite. However, it is also possible to find tricalcium phosphate, calcium carbonate and fluoride derivatives in this matrix [30]. The mineral component of bone provides tensile yield strength and it is also involved in functions related to the ions' storage [26]. It is estimated that the bones contain 99% of the calcium, 85% of phosphorous and 40-60% of magnesium and sodium found in the human body [31].

The equilibrium between the organic and inorganic phases of the bone matrix is crucial. Indeed, when the mineral component is reduced, the bone becomes more flexible due to the increase of collagen. Otherwise, if the amount of collagen is low, the bone become very brittle due to the high mineral fraction [5, 32, 33].

### 1.3.2. Bone cells

In the bone tissue maintenance and remodelling processes, the action of the bone cells (osteoblasts, bone lining cells, osteocytes and osteoclasts), represented in Figure 2, is crucial.

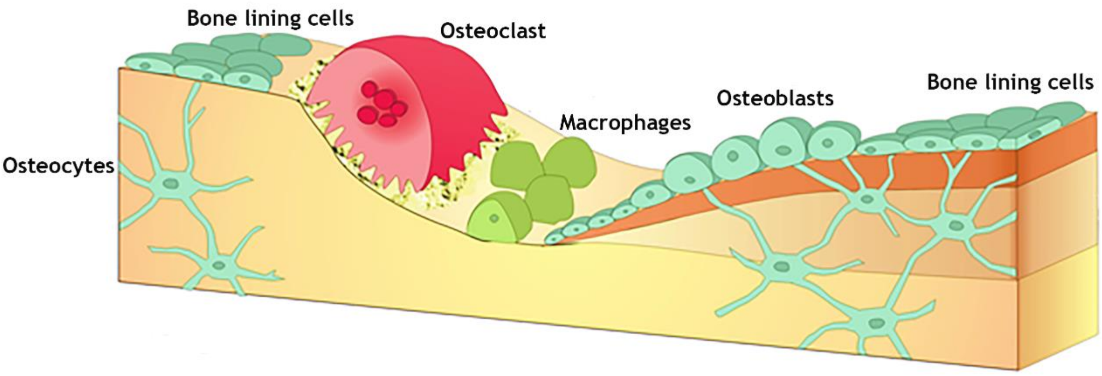

**Figure 2.** Schematic representation of the cells found in bone tissue. Osteoblasts are involved in bone formation; Bone lining cells can become differentiated into osteogenic cells; Osteocytes are responsible for the maintenance of the integrity of bone tissue; Osteoclasts are involved in bone resorption (adapted from [34]).

#### 1.3.2.1. Osteoblasts

Osteoblasts cells are derived from mesenchymal stem cells (MSCs) and are located essentially in bone marrow and periosteum [13]. They have a cube-like shape or a slightly elongated appearance and present enlarged organelles (like nucleus, Golgi and endoplasmic reticulum apparatus) which play a pivotal role in the synthesis and organization of bone ECM [33]. Additionally, osteoblasts also participate in bone mineralization, through the release of the calcium ions and enzymes (e.g. alkaline phosphatase) from its vesicles [35]. The lifespan of osteoblasts is about 8 weeks in the human body. When they become differentiated, osteoblasts may have distinct fates: revert back to bone lining phenotype, differentiate into osteocytes or undergo apoptosis [31].

#### 1.3.2.2. Bone lining cells

After the bone formation process occurs, some osteoblasts differentiate into osteocytes, while other cells remain at quiescent state at the bone surface, being nominated as bone lining cells (BLCs). BLCs contain few cell organelles, present flat or slightly ovoid nuclei, and are thinly extended over the bone surfaces [4, 36].

BLCs can be differentiated into osteogenic cells, representing a source of "determined" osteogenic precursors [37]. BLCs can also be involved in hematopoiesis as well as activate the bone resorption and remodelling process. Some evidences also suggest that the BLCs are important for the regulation of the influx and efflux of mineral ions [12]. In addition, BLCs secrete enzymes that recruit osteoclasts to specific sites of bone surface, that stimulate the bone resorption [12, 36, 37].

#### 1.3.2.3. Osteocytes

Osteocytes are the most abundant cell type in bone. They are formed through a process that involves osteoblasts differentiation and form a syncytial network that supports bone structure and metabolism [31, 38]. Morphologically, osteocytes display a stellate shape, with a reduced endoplasmic reticulum, mitochondria and a single nucleus [39]. Osteocytes lie within lacunae in mineralized bone and have cytoplasmic extensions that allow the connection between the cells [12, 40, 41].

Osteocytes act as mechanosensors that are capable of transducing musculoskeletal signals, that guide the bone remodelling process. Some authors suggested that the signalling mechanisms involved in mechanotransduction include nitric oxide, Wnt and cadherin-mediated signalling [42, 43]. Despite of osteocytes may live for decades in human bone, these cells may undergo apoptosis in aging bone, probably due to the disruption of their intercellular gap junctions or cell-matrix interactions [12].

#### 1.3.2.4. Osteoclasts

Osteoclasts are derived from hematopoietic stem cells and they are responsible for the reabsorption of fully mineralized bone. Osteoclasts are giant multinucleated cells, containing abundant mitochondria, a well-developed Golgi apparatus around the nuclei, endoplasmic reticulum and a high number of vacuoles and lysosomes [44]. These cells participate in skeletal development and in the resorption of fully mineralized bone, leading to the mobilization of calcium ($Ca^{2+}$) and phosphate ($PO_4^{3-}$) ions from the bone matrix [13, 26]. Further, osteoclasts are responsible for bone resorption through the secretion of acid and collagenase [12]. During their motile state, these cells migrate from the bone marrow to resorptive site, where the bone resorption begins. In this state, the osteoclasts are flattened, non-polarized cells, and are characterized by the presence of membrane protrusions, called lamellipodia, and podosome complexes containing actin. When they reach the resorptive site, osteoclasts become polarized, through a process that involves cytoskeletal reorganization. Such process leads to the formation of specific membrane domains, that separates the acidic resorptive environment from the rest of the cell. During the resorption, osteoclasts are dome-shaped and lack lamellipodia [38, 45].

An activated osteoclast is able to resorb 200 000 $\mu m^3$/day of bone matrix, within an average lifespan of 15-20 days [13]. However, their abnormal activity leads to some bone diseases, such as osteomyelitis and osteoporosis [4].

## 1.4. Bone regeneration process

Bone is a dynamic tissue, capable to self-regenerate. However, this capacity may be compromised when fractures occur in unfavourable anatomical positions, showing a delay in healing or even develop pseudo-arthrosis or non-unions. Several factors affect the bone repairing process and can be classified according to the extent of tissue loss [2, 46]. In this way, bone repair (Figure 3) can be defined into two categories: primary (direct) and secondary (indirect) bone healing.

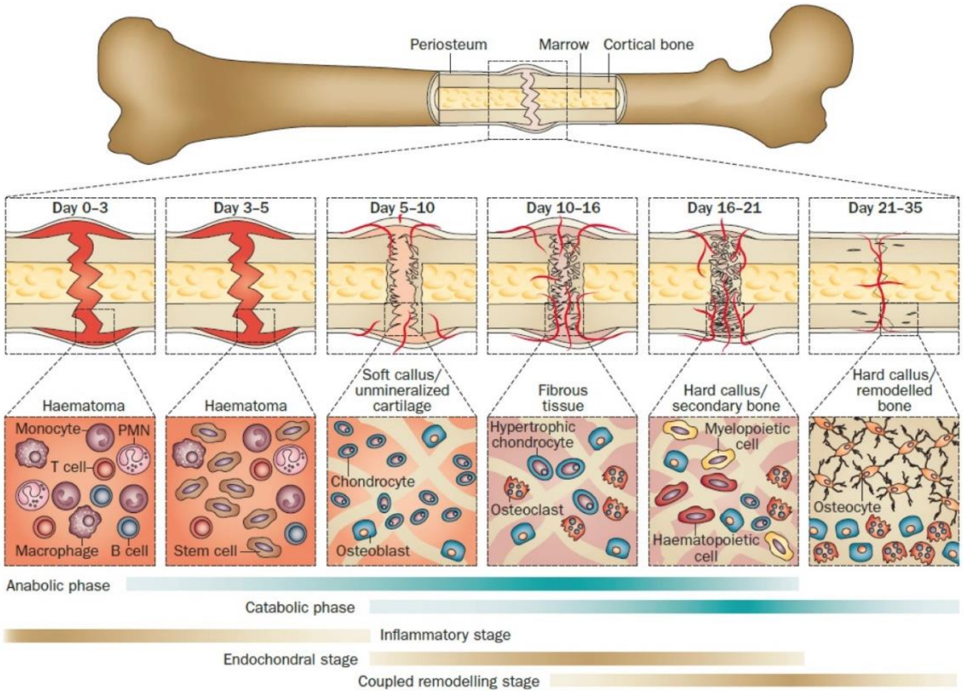
Periosteum
Marrow
Cortical bone
Day 0–3
Day 3–5
Day 5–10
Day 10–16
Day 16–21
Day 21–35
Haematoma
Haematoma
Soft callus/ unmineralized cartilage
Fibrous tissue
Hard callus/ secondary bone
Hard callus/ remodelled bone
Monocyte
PMN
T cell
Macrophage
B cell
Stem cell
Chondrocyte
Osteoblast
Hypertrophic chondrocyte
Osteoclast
Myelopoietic cell
Haematopoietic cell
Osteocyte
Anabolic phase
Catabolic phase
Inflammatory stage
Endochondral stage
Coupled remodelling stage

**Figure 3.** Illustration of the typical fracture healing phases (reproduced from [47]).

### 1.4.1. Primary (direct) bone healing

In general, the primary bone healing occurs when the fracture gap is smaller than 0.1 mm and the fracture site is rigidly stabilized [22]. In this process, the bone gap is filled through the continuous ossification and subsequent Harversian remodelling, without occurring the formation of the cartilaginous or connective tissue [48]. In this type of healing, the fracture union can occur by contact healing or gap healing.

In contact healing, the gap between bone ends is less than 0.01 mm and interfragmentary strain is smaller than 2% [49]. In this process, the bone matrix is produced through the action of the osteoblasts and simultaneously, the bony union and Haversian systems are re-established in an axial direction. Such event allows the penetration of blood vessels that carry osteoblastic precursors. Later, the remodelling into lamellar bone occurs, resulting in fracture healing without occurring the formation of periosteal callus [49, 50].

On the other side, when the gap between fracture ends is less than 800 µm – 1 mm, the bony union and Haversian remodelling do not occur simultaneously. Initially, the fracture site is filled with lamellar bone which is mechanically weak. After, a secondary osteonal reconstruction occurs to fully restore the anatomical and biomechanical properties of the bone [49].

### 1.4.2. Secondary (indirect) bone healing

Indirect bone healing is the most common type of bone healing and it involves several events, such as blood clotting, inflammatory response, fibrocartilage callus formation, intramembranous and endochondral ossification, and bone remodelling [48].

Immediately after a trauma occurs, a haematoma is produced in order to act as template for callus formation. Such event starts the inflammatory response, where proinflammatory molecules (such tumour necrosis factor-α (TNF-α), interleukin-1 (IL-1) and interleukin-6 (IL-6)) play an important role in the recruitment of inflammatory cells and in the promotion of the angiogenesis [48, 49]. Subsequently, the MSCs are recruited to the injured site, where they proliferate and differentiate into osteogenic cells, through the action of osteoinductive molecules (such as BMPs). These molecules are also involved in the hard callus development, since they stimulate bone formation [51, 52].

After the formation of the primary haematoma, a fibrin-rich granulation tissue is produced, and the endochondral formation occurs between the fracture ends. Then, the cartilaginous tissue forms a soft callus, in order to stabilize the fracture. Simultaneously, an intramembranous ossification response occurs, generating a hard callus that provides a semi-rigid structure to the fracture [53]. Afterwards, the revascularization and blood supply processes are initiated [54]. Subsequently, the resorption of primary soft callus and their replacement by a hard bony callus occurs. In this process, ECM becomes calcified as a result of the hypertropia of the chondrocytes. In turn, the mitochondria is responsible for the calcification mechanism through the accumulation of calcium-containing granules, which are involved in the production of the mineral deposits [55]. Such deposits of calcium and phosphate trigger the nucleation process which leads to the formation of apatite crystals. The progression of the hard callus formation results in the replacement of the calcified cartilage in woven bone, becoming the callus more solid and mechanically rigid [49, 56]. After that, the fully restoration of the biomechanical properties of native bone is achieved through a second resorptive phase. In this phase, the hard callus is remodelled into a lamellar bone structure with a central medullary cavity. The remodelling process is performed by a balance of hard callus resorption by osteoclasts, and lamellar bone deposition by osteoblasts [49].

## 1.5. Bone Disorders

The bone healing process is sometimes compromised by different circumstances, such as pathologies that compromise the structural and functional integrity of the bone. The abnormal collagen contents can lead to osteogenesis imperfecta and deficiencies in mineral and vitamin content, leading to rickets or osteoporosis [38, 57, 58]. In turn, bacterial infections can cause osteomyelitis [59]. Figure 4 represents an overview of the most common disorders associated with bone tissue.

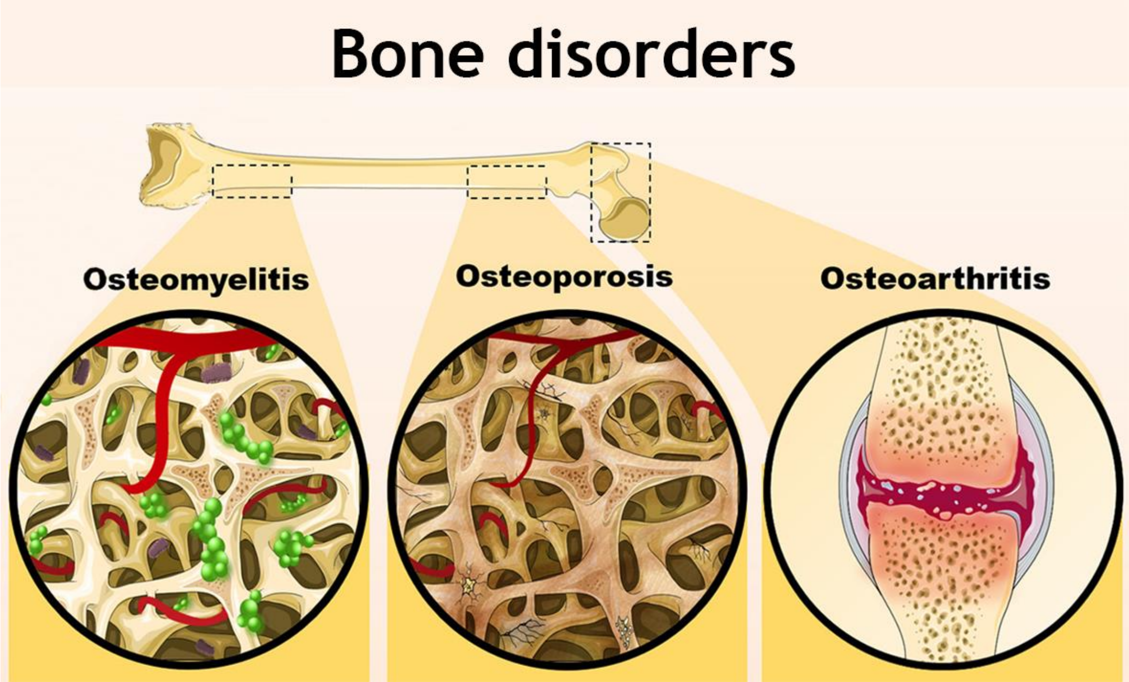

**Figure 4.** Representation of the main disorders that affect the bone tissue (adapted from [60]).

### 1.5.1. Osteoporosis

Osteoporosis is the most common bone disease and it is characterized by an increased bone resorption, that leads to a decrease of bone mineral density. Such events increase the bone fragility and risk of fractures [61]. It has been verified that elderly populations, especially women, are the most affected by osteoporosis. [45, 58]. The most common osteoporotic fractures affect the hip, vertebral column and forearm. Such fractures are responsible for morbidity or ultimately, in severe cases, for patient death. Unhealthy diet, sedentary lifestyle, nulliparity, aging, smoking, and low body weight have been identified as risk factors that may trigger the development of osteoporosis [9, 45].

### 1.5.2. Pagets' Disease

Paget's disease is the second most common type of metabolic bone disease [38]. This disease is characterized by focal areas of excessive bone resorption alternated with areas of increased bone formation, causing the formation of an abnormal bone, pain, pathologic fractures, deafness and nerve compression syndromes [45, 62]. This disease is more prevalent in humans with an age over 40 years [63]. In this pathology, the osteoclast precursors exhibit increased sensitivity to factors that stimulate bone resorption including RANKL. It is proposed that genetic factors and gene mutations have an important role in this disease. However, environmental factors and sedentary lifestyle are also related with the Paget's disease [64].

### 1.5.3. Osteomyelitis

Osteomyelitis is an inflammation of bone and bone marrow caused by a microbial infection that leads to the destruction of the bone tissue. However, it can also be triggered by fractures arising from trauma or other diseases [59, 65]. *Staphylococcus aureus* (*S. aureus*) is the most common pathogen responsible for the emergence of this disease. This microorganism grows in biofilm, which protects bacteria from antimicrobial treatment and from the host immune response. Furthermore, it is able to produce a wide range of extracellular components and cell-associated factors, that increase its colonization capacity and virulence [59].

### 1.5.4. Osteoarthritis

Osteoarthritis is the most common degenerative joint disease and a major cause of pain and disability in adults [66]. Osteoarthritis is characterized by an irregular remodelling of joint tissues due to the presence of inflammatory mediators. This disease causes progressive loss and destruction of articular cartilage, mobility limitations and different degrees of local inflammation. It can affect any joint, but commonly appear in the hip, knee and the joints of hand, foot and spine [66, 67]. Osteoarthritis disease has been associated with multifactorial factors as joint injury, obesity, aging and heredity [66].

## 1.6. Bone Grafts

Bone grafting is a procedure commonly used in surgery to enhance the regeneration of injured bone [46]. Bone grafts can be classified into autografts, allografts and xenografts. The autografts involve the removal of an osseous graft harvested from an anatomic site and transplanted into another site within the same individual [46]. Due to the osteoconductive, osteoinductive and osteogenic properties displayed by an autologous bone graft, it be can integrated within the host bone without eliciting any side effects. Considering these attractive properties, these bone grafts have been regarded as the gold standard for treating bone defects [48]. However, the handicaps of autografts have been extensively reported, and are related to the harvesting process, including donor site complication and pain, increased blood loss, risk of donor site infection and low availability of the material [48, 68].

To overcome these handicaps, allografts and xenografts arised as a therapeutic alternative used by surgeons. Allogeneic bone graft is harvested from one individual and transplanted to a genetically different individual of the same species. This type of grafts is considered the best alternative to autografts, especially for those patients with poor healing capacity, and established nonunion. Although, allografts can be immunogenic and demonstrate a higher failure rate, which can be caused by the activation of the major histocompatibility complex (MHC) antigens [48, 69].

Ultimately, as a last resort, xenografts are used in patients who demand for large amounts of tissue transplantation. These grafts are usually obtained from animals and they may be associated with virus transmission, infection, toxicity, immunogenicity, and host rejection [69].

Hence, the limitations displayed by the bone grafts, have triggered the research and development of alternative bone repair approaches in the area of Tissue Engineering (TE). This emerging area intends to develop three dimensional (3D) structures capable of mimicking the native bone structure and provide a suitable microenvironment for bone regeneration process occur [68].

## 1.7. Tissue Engineering

TE is a relatively new interdisciplinary field that applies the principles of engineering and life sciences towards the development of biological substitutes that repair, maintain or improve damaged tissue structure and functions [70]. In particular, Bone Tissue Engineering (BTE) has been focused on the production of the bone substitutes that are capable of inducing the re-establishment of bone structure and functions (as illustrated in Figure 5).

BTE has been focused in the development of new personalized bone substitutes, with high potential to be used as medical devices. The bone substitutes have been produced with natural/synthetic polymers, ceramics, metals and/or composite materials. Further, the bone substitutes can be functionalized with cells, nanoparticles, growth factors or other bioactive molecules [6, 8, 70, 71].

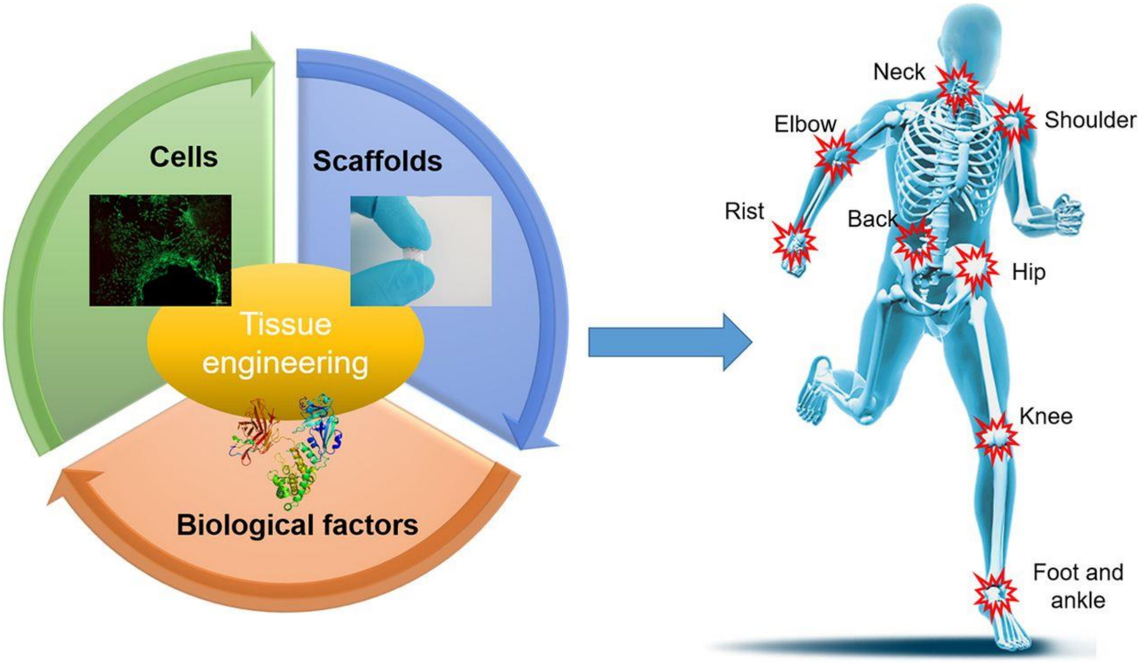

**Figure 5.** Representative illustration of the main strategies used in the Bone Tissue Engineering (reproduced from [72]).

### 1.7.1. Properties exhibited by 3D scaffolds aimed for bone regeneration

In recent years, a huge effort has been done to produce ideal structures that can be used for bone regeneration. These 3D structures are known as scaffolds, which are conceived to provide enough mechanical support while guiding cell migration, proliferation and differentiation, as well as to deliver bioactive molecules [6, 70]. For BTE applications, an ideal scaffold must fulfil the following set of specific properties.

#### 1.7.1.1. Biocompatibility

The biocompatibility is the most important feature that any scaffold aimed for TE must display [73]. Biocompatibility refers to the ability of a material to support cellular events, including adhesion, proliferation and cell differentiation as well as improve the vascularization and do not elicit any inflammatory effect on the host tissue [46, 73, 74]. Scaffolds' biocompatibility is influenced by type of the materials used and its chemical structure, which should generate the most appropriated tissue response [75]. Moreover, the products resulting from the scaffolds' degradation must be naturally removed from the body, without induce any toxic effect for the body [46, 73].

#### 1.7.1.2. Biodegradability

The scaffolds can be design according to the pretended biomedical application to act as permanent or temporary implants [6]. The temporary structures are the most investigated due to their capacity to exhibit different degradation rates. Scaffolds' degradation rates should match the regeneration rate of bone native tissue. Materials' degradation can be triggered by physical or chemical processes or even by biological processes, mediated by enzymatic mechanisms. Moreover, the designed scaffold should be nontoxic and must be able to get metabolized and eliminated from the body [71, 73, 75].

#### 1.7.1.3. Surface properties, osteoconductivity and osteoinductivity

The success of the scaffold implantation is dependent on the scaffolds' surface properties such as charge, chemical composition, roughness, softness, stiffness and hydrophilicity/hydrophobic character [76]. Such features have a significant impact on the regulation of cellular adhesion and proliferation, which are also directly related with the osteoconductivity and osteoinductivity exhibited by scaffolds. Osteoconductivity reflects the ability of a scaffold to support the attachment of osteoblasts or osteoprogenitor cells, as well as to provide a suitable interconnected structure that favours cell migration and angiogenesis processes [71, 77]. In turn, osteoinductivity represents the capacity of a scaffold to promote the differentiation of the osteoprogenitor cells into osteoblasts. Such property is crucial, since it triggers the bone formation process and, consequently, improve the bone tissue regeneration [6, 73]. Several findings evidenced that the rough and positively charged surfaces promote the osteoconduction, creating a matrix that enhances cell adhesion and proliferation [73]. On the other hand, the scaffolds may be loaded with osteoinductive signals (growth factors or other bioactive molecules) that induce differentiation of bone cells [73].

#### 1.7.1.4. Mechanical Properties

3D structures aimed for bone regeneration must provide adequate mechanical support at the lesion site until the new bone is entirely matured [46, 73]. Specifically, in the case of bone tissue, the mechanical properties of scaffolds, including stiffness and compressive strength, must be compatible with those presented by the native bone. Cortical bone presented a Young modulus values comprehended between 15-20 GPa, while trabecular bone presents a value between 0.1-2 GPa [71]. Regarding to the compressive strength values, cortical and trabecular bone displays 100-200 MPa and 2-20 MPa, respectively [71].

Moreover, the scaffolds must be tailored for a specific application, since these properties are dependent on the bone type and location. Additionally, it is required a balance between the mechanical properties displayed by the scaffold and its degradation rate, therefore scaffolds must grant support until the new bone is formed [46, 73].

#### 1.7.1.5. Porosity

Porosity represents the percentage of void spaces available within the scaffolds' structure. Scaffolds must display interconnected porous structure that favours nutrients and cells exchange, which is crucial for the maintenance of cell viability as wells as promoting bone regeneration [71, 73]. A scaffold is considered ideal, when it exhibits a similar porosity to that displayed by trabecular bone (50-90%), allowing cell infiltration, differentiation and, consequently improve the new bone tissue formation [78]. In addition, scaffold must possess pores with a pore size comprehended between 100-300 µm, in order to promote cells migration, essential nutrients, oxygen and cellular metabolites exchange [71, 78].

However, the pore size and distribution must be tailored in order to preserve the biological functions and mechanical stability of scaffolds. It is well known that highly porous scaffolds, tend to have a lower mechanical resistance and to exhibit higher degradation rates [73].

#### 1.7.1.6. Antibacterial activity

One the most severe and devastating complications associated with the implantation of bone implants is the occurrence of bacterial contamination [79]. Nowadays, it is estimated that 65-80% of bacterial infections arise from the microorganisms that form biofilms on implants' surface, compromising their successful application [79, 80]. Additionally, it is reported that *S. aureus* strain is responsible for 30% of all implant infections [79]. In turn, *Escherichia coli* (*E. coli*) is one of the first causes of gram-negative implant infections, with a prevalence of 23%, in 155 studied cases [81, 82].

To surpass this severe complication, the researchers have been exploring different functionalization strategies in order to confer antimicrobial activity to the scaffolds. The incorporation of the antibacterial agents (e.g. metallic nanoparticles, antibiotics, antimicrobial polymers, etc.) into bone scaffolds has been performed [83].

### 1.7.2. Techniques used for scaffold fabrication

The methods used for scaffolds manufacturing are categorized in conventional (salt leaching, gas foaming, phase separation, vapor deposition and freeze-drying) and rapid-prototyping (RP) (fused deposition modelling, selective laser sintering and stereolithography) techniques [84-88]. The conventional methods do not enable the precise control of internal scaffold architecture or the fabrication of scaffolds with a complex geometry [89].

On the other side, RP procedures trigger the interest of researchers, due to its reproducibility and accuracy. These techniques enable the production of 3D structures with appropriate mechanical properties using CAD/CAM software. Further, the scaffolds with the precise shape and size of bone defects can be produced by combining RP with imaging techniques, allowing the production of personalized therapeutic solutions [84]. 3D plotting is one of the most used RP techniques in area of BTE [18]. In this process, a blend is dispensed onto a platform, through a syringe. The deposition can be achieved by pneumatic action, screw-driven, or piston action [90].

In this work, Fab@Home 3D plotter was used to produce the scaffolds, following a protocol described by our group [91-93].

#### 1.7.2.1. Scaffold fabrication with a Fab@Home 3D Plotter

The Fab@Home printer presents advantages over other equipment, since it allows the use of wide range of materials, such as composites comprising ceramics and polymers. The deposition of successive layers to produce the final 3D model, allows to control of pore sizes, morphology, and overall matrix porosity in comparison to other fabrication methods [94].

During the printing process, the syringe content is compressed to extrude the 3D structure onto a platform, according to the CAD file. The printing accuracy is dependent on the viscosity, dispensing pressure, pushout (early dispensing before cartridge starts to move along the printing path), suckback (sets how much the plunger withdraws at the end of the printing path to stop the extrusion process), nozzle diameters (determines the resolution of the printing process), deposition rate (determines the amount of material deposited for each mm of printing path), printing speed (speed at which the cartridge moves along the printing path), path height (distance between consecutive layers) and path space (space between adjacent printing paths), set in the equipment [95, 96]. Thus, this feasible, cheap and reproducible technique enables the production of complex 3D structures with high resolution and with a controlled internal architecture. Moreover, the templates produced by this method exhibit higher mechanical properties which are crucial to fulfill the demands for bone repair applications [97].

## 1.7.3. Biomaterials used for scaffold fabrication

The selection of the materials used for scaffold production is crucial, since this selection will influence the final properties of the scaffold [70, 73]. So far, different materials have been used for this purpose, including metals, natural and synthetic polymers as well as composites.

### 1.7.3.1. Metals

Metals are known by its great compressive strength, ductility, tenacity and hardness. The most common metal used in scaffolds production is Titanium (Ti). However, metal implants have associated several complications such as infections or excess of fatigue loading. Further, the use of metallic implants can lead to the release toxic ions (due to corrosion) causing inflammation and tissue loss [78, 98].

### 1.7.3.2. Ceramics

Ceramic scaffolds are commonly characterized by displaying high mechanical stiffness, low elasticity and a hard surface [99]. Up to now, hydroxyapatite (HA) and tricalcium phosphate (TCP) have been the most used ceramics for scaffolds production [100]. These bioactive ceramic materials exhibit excellent biodegradability and biocompatibility, due to their chemical and structural resemblance with the mineral phase of native bone [73]. Additionally, the ceramics promote interactions with osteogenic cells, improving osteoblasts differentiation, and proliferation. It is also described that bioactive ceramics induce mineralization at scaffolds' surface, increasing their biointegration and, consequently, the bone regeneration process [73, 101].

**Tricalcium phosphate**

TCP is a ceramic widely used in the BTE, since it is biodegradable, biocompatible and osteoconductive. Furthermore, its low price and degradation rate (it has a 10 times higher degradation rate than that exhibited by hydroxyapatite), supports its application in BTE.

Moreover, TCP scaffolds present a mechanical strength that is compatible with the requirements of native bone. Santos and co-workers produced TCP scaffolds and their results showed that the scaffolds were able to promote a good interaction with cells [102]. However, TCP or ceramic scaffolds have some limitations associated, namely the relative brittleness and poor resistance to fatigue [103].

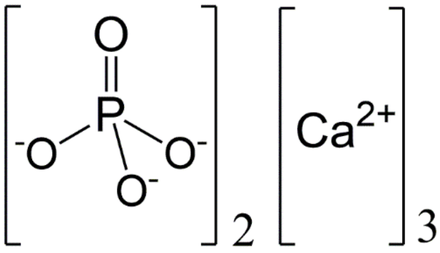

**Figure 6**. Chemical structure of tricalcium phosphate.

### 1.7.3.3. Polymers

Polymers are macromolecules that present remarkable biological properties, like biodegradability, biocompatibility, bioactivity [73, 104]. Such properties make them very attractive for BTE applications. The polymers, according to their source, can be classified as natural and synthetic [75, 104].

#### 1.7.3.3.1. Natural Polymers

Natural polymers are obtained from natural sources, such as plants and animals. A large variety of natural polymers have been applied in BTE, including proteins (silk, collagen and gelatin) and polysaccharides (alginate, chitin/chitosan and cellulose) [105]. As main advantages of these materials are their low immunological potential, biocompatibility and structural similarity with bone organic matrix [106]. Nonetheless, the use of naturally derived polymers presents some limitations, including their weak mechanical behaviour, fast degradation rates as well as hard processing and purification [107].

**Gelatin**

Gelatin (Gel) is a natural and cheap biopolymer, which is obtained from the hydrolysis of collagen [108]. It is composed by three aminoacids, glycine, proline and 4-hydroxyproline residues [109]. So far, this polymer has been used in production of pharmaceuticals, cosmetics and food products. In TE, the increasing interest on this material relies on its biological properties such as biodegradability and biocompatibility. In addition, Gel presents low antigenicity, physico-chemical stability as well as specific binding domains, known as arginine-glycine-aspartic acid (RGD) sequences. Such sequences play a crucial role in cell adhesion to the biomaterial, since integrins receptors available on cell membrane are able to recognize these aminoacid sequences [109-111].

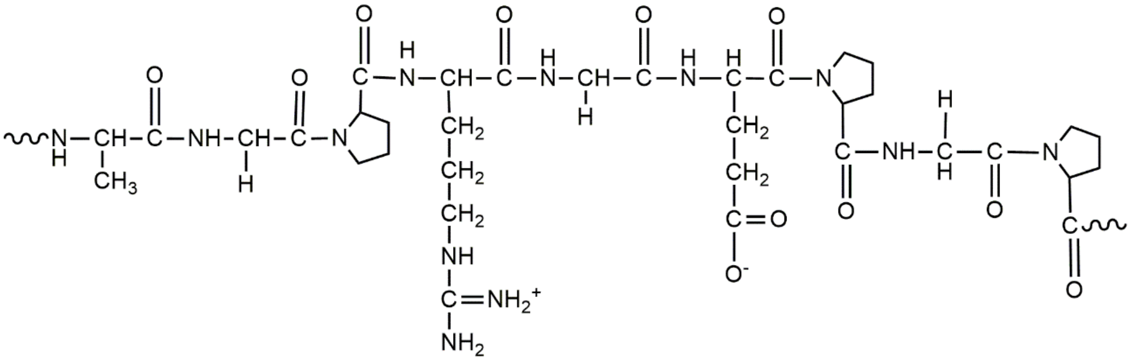

**Figure 7.** Chemical structure of gelatin.

## Chitosan

CH is a natural cationic polymer, which is attained from the alkaline deacetylation of chitin (the second most abundant polymer on Earth after cellulose) that is usually obtained from the exoskeleton of the crustaceans, such as shrimp, crab and lobster [112, 113]. This polysaccharide is composed by glucosamine and N-acetyl glucosamine units linked by ß (1-4) glycosidic bonds [113, 114].

CH is also characterized by being bioactive, biodegradable, bioadhesive, hemostatic and displaying antimicrobial activity. Such features make this polymer a highly promising biomaterial for being applied in the area of TE [112]. As a natural biodegradable polymer, CH can be enzymatically degraded through lysozyme and chitosanase, being its degradation rate controlled by factors like temperature, ionic strength and pH [115, 116].

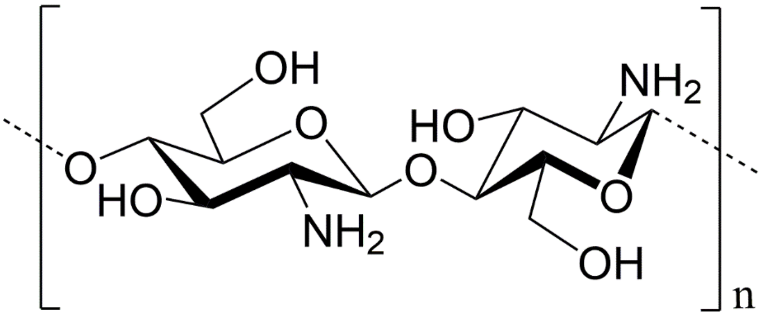

**Figure 8.** Chemical structure of chitosan.

### 1.7.3.3.2. Synthetic Polymers

Synthetic polymers are chemically synthetized and they are used in BTE, due to their high versatility and reproducibility [71, 73]. In general, the synthetic polymers possess excellent mechanical properties, although they are less biocompatible than natural polymers. Polylactic acid (PLA), polyglycolic acid (PGA), poly(lactic-co-glycolic) acid (PLGA) and polycaprolactone (PCL) are examples of synthetic polymers that have been used BTE field [73].

### 1.7.3.4. Composites

The search of bone substitutes that are capable of fulfilling all the requirements of bone tissue have triggered the combination of different materials to obtain scaffolds with a set of specific properties [117, 118]. These materials are characterized by having a dispersed (essentially composed by ceramics) and matrix (comprised of polymers) phases. The dispersed phase acts as support of the matrix phase, providing resistance, stiffness, osteoconductivity and mimicking the natural minerals found in native bone. In turn, the matrix phase reproduces the biological interactions presented in the bone native ECM [78, 119].

### 1.7.3.5. Graphene-based materials

In recent studies, researchers have incorporated graphene-derived materials into the structure of 3D scaffolds, in order to improve the mechanical and osteogenic properties of the scaffolds aimed for bone regeneration. The graphene oxide (GO) and its chemical derivatives have showing promising properties for application in TE. The next sub-sections describe the properties of these nanomaterials [120, 121].

### 1.7.3.5.1. Graphene Oxide

GO is composed by a graphitic lattice with several types of oxygen-functional groups, such as hydroxyl, carboxyl or epoxy [122]. The synthesis of this material comprises two main steps. First, graphite is chemically oxidized into graphite oxide. Afterwards, graphite oxide is exfoliated by sonication, resulting in the production of GO [123, 124]. The oxygen-functional groups of GO endow it a good hydrophilicity and dispersibility in water. On the other hand, the aromatic matrix of GO allows the incorporation of bioactive agents on this nanomaterial through hydrophobic interactions or π-π stacking. Furthermore, GO high surface area and mechanical properties have also triggered the interest on this nanomaterial [125, 126].

In BTE applications, GO has been incorporated into 3D scaffolds in order to improve the physico-chemical and mechanical properties of the scaffolds aimed for bone tissue engineering. In fact, Boga *et al.* demonstrated that the incorporation of GO into 3D printed scaffolds can improve their compressive strength by 4-fold [121]. In the same study, authors also verified that GO could enhance the porosity of the scaffolds without compromising the mechanical integrity of the construct [121]. Besides these properties, the presence of GO in scaffolds can induce the differentiation of stem cells, and also improve the biomineralization process [127, 128]. Furthermore, other studies have also demonstrated the biocompatibility and biodegradability of GO [122, 129], properties that make this material suitable to be used in BTE applications.

#### 1.7.3.5.2. Reduced Graphene Oxide

Reduced graphene oxide (rGO) is obtained through the reduction of GO by thermal or chemical processes, being the last the most commonly used [130, 131]. The reduction of GO aims to restore its aromatic lattice (by removing the oxygen-functional groups), yielding a material with significantly different properties in comparison to its precursor [130]. For instance, Kanayama *et al.* coated the surface of collagen scaffolds with rGO, revealing that they display a greater compressive strength, a higher calcium adsorption and a high alkaline phosphatase activity, when compared to their equivalents containing GO [132].

Despite the potential of rGO, the direct incorporation of this material in the structure of 3D scaffolds is hindered by several factors. rGO is generally attained by treating GO with hydrazine hydrate, being this a highly hazardous reducing agent [131, 133]. To address this limitation, GO can also be reduced by environmentally-friendly methods, like performing the treatment of GO with L-Ascorbic Acid (LAA or Vitamin C) for removing its oxygen-functional groups (reduction) and yields a material with a good biocompatibility [134, 135].

Nevertheless, independently of the method selected to produce rGO, the hydrophobic character of this material hinders its incorporation in 3D scaffolds. In fact, rGO is not soluble in water, suffering aggregation during the reduction process [136, 137]. Therefore, it is crucial to develop new methods that allow the obtention of rGO with suitable properties to be used in the functionalization of 3D printed scaffolds.

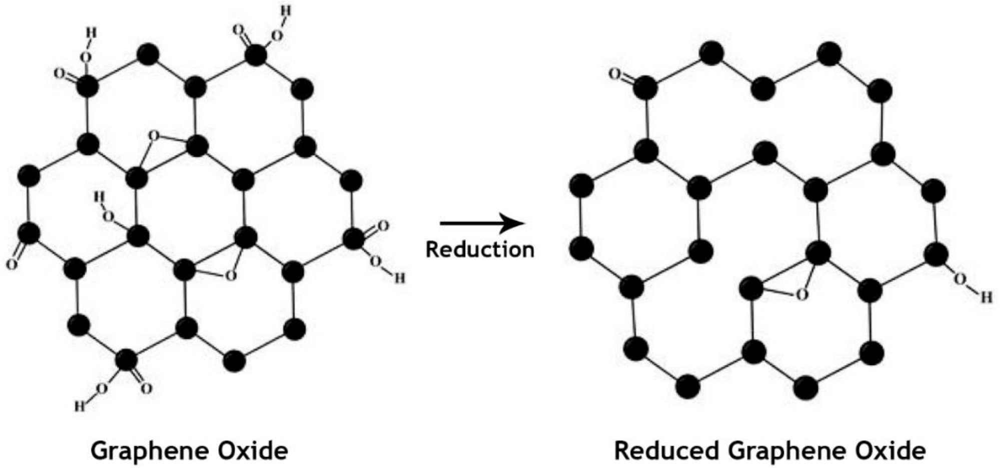
Reduction
Graphene Oxide
Reduced Graphene Oxide

**Figure 9.** Chemical structure of graphene oxide and reduced graphene oxide (adapted from [138]).

## 1.8. Aims

The overall aim of the present thesis workplan was to produce and characterize 3D bioactive scaffolds functionalized with rGO aimed to be used for bone tissue regeneration applications.

The specific objectives of this study were:

- Optimization of the blends composition (TCP, Gel and CH) to be used in scaffold production;
- Production and functionalization of scaffolds with rGO (TGC_irGO), through *in situ* reduction method, using LAA as reducing agent;
- Production of TGC and TGC_GO scaffolds for comparative purposes;
- Evaluation of the mechanical, physico-chemical and biological properties of the produced scaffolds.

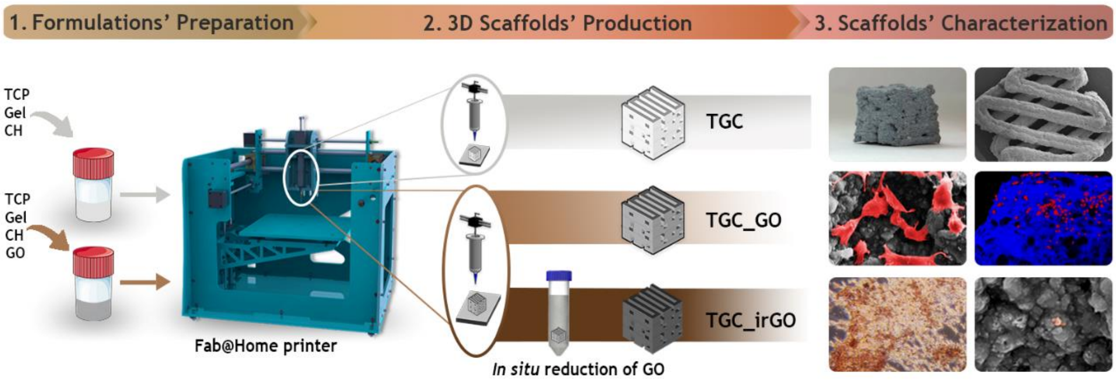
1. Formulations' Preparation
2. 3D Scaffolds' Production
3. Scaffolds' Characterization
TCP
Gel
CH
TCP
Gel
CH
GO
Fab@Home printer
TGC
TGC_GO
TGC_irGO
In situ reduction of GO

**Figure 10.** Schematic representation of the experimental setup used to produce TGC, TGC_GO and TGC_irGO scaffolds. (1) Preparation of the composite formulations (TCP, Gel, CH and GO); (2) Production of 3D scaffolds using a Fab@Home printer; (3) Evaluation of the physico-chemical, biological and antibacterial properties of the 3D produced scaffolds.

# Chapter II

# 2. Materials and Methods

## 2.1. Materials

Alizarin Red S, alkaline phosphatase, chitosan medium molecular weight (190 000-310 000 Da; degree of deacetylation: 83.35% ± 0.23), Dulbecco's modified Eagle's medium (DMEM-F12), ethylenediaminetetraacetic acid (EDTA), diethanolamine, gelatin 160 bloom, glutaraldehyde 25% (v/v), LB broth, hydrochloric acid (HCl), *p*-Nitrophenylphosphate (pNPP), paraformaldehyde (PFA), phosphate buffered saline solution (PBS), sodium hydroxide (NaOH), sodium tripolyphosphate (TPP), triton X-100 and trypsin were purchased from Sigma-Aldrich (Sintra, Portugal). Graphene oxide (GO) was obtained from NanoPoz (Umultowska Poznan, Wielkopolska). Lysozyme from chicken egg was acquired from Alfa Aesar (Haverhill, MA, USA). Acetic acid was acquired from Pronalab (Barcelona, Spain). Normal human osteoblast (hOB; 406-05f) cryopreserved cells were bought to Cell Applications, Inc. (San Diego, USA). *Staphylococcus aureus* clinical isolate (*S. aureus*; ATCC 25923) and *Escherichia coli DH5a* (*E. coli*) were used to evaluate antimicrobial properties of scaffolds. Fetal bovine serum was provided by Biochrom AG (Berlin, Germany). 3-(4,5-dimethylthiazol-2-yl)-5-(3-carboxymethoxyphenyl)-2-(4-sulfophenyl)-2H-tetrazolium (MTS) was bought to Promega (Madison, WI, USA). Propidium Iodide buffer was acquired from Life Technologies (Maryland, USA). Tris base and L-Ascorbic acid (LAA) were obtained from Fisher Scientific (Porto Salvo, Portugal). Tricalcium phosphate (TCP) was purchased from Panreac (Barcelona, Spain). Double deionized and filtered water was obtained using a Milli-Q Advantage A10 ultrapure Water Purification System (0.22 μm filtered; 18.2 MΩ/cm at 25 °C).

## 2.2. Methods

### 2.2.1. Preparation and characterization of GO and rGO (direct reduction with LAA)

The commercial GO solution was purified by dialysis against water for 3 days (14 kDa molecular weight cut-off membrane) and subjected to sonication cycles in order to obtain nano-sized GO. GO was also treated with LAA (10 mM) for 24 h, at 40 ºC (30 rpm) to obtain rGO by direct reduction.

The size distribution of GO was determined by Dynamic Light Scattering (DLS), using a Zetasizer Nano ZS (Malvern Instruments Ltd., Worcestershire, UK), at a scattering angle of 173°. GO and rGO (direct reduction with LAA) were also characterized by Attenuated Total Reflectance-Fourier Transform Infrared Spectroscopy (ATR-FTIR). Spectra were acquired with an average of

128 scans, between 400 and 4000 $cm^{-1}$ and with a spectral resolution of 32 $cm^{-1}$ [139]. Then, the powdered samples were mounted on a diamond window, and the analysis was conducted on a Nicolet iS10 FTIR spectrophotometer (Thermo Scientific, Waltham, MA, USA).

The elemental composition of the samples was also determined by Energy Dispersive Spectroscopy (EDS). For this purpose, samples were placed on aluminium stub supports, air-dried at room-temperature (RT) and then analyzed in a XFlash Detector 5010 (Bruker Nano, Germany).

### 2.2.2. Production of TGC_irGO scaffolds

TGC_irGO scaffolds were produced as illustrated in Figure 11 A. To accomplish that, the TCP (an inorganic compound) and the Gel/CH (organic elements) were combined at a ratio of 80/20 (w/w), in order to mimic the phases found in the native bone. Initially, the CH (800 mg in 15 mL of acetic acid solution (1% (v/v)) and Gel (150 mg in 1 mL of water at 50 ºC) solutions were thoroughly mixed, by using an X10/25 Ultra-turrax. Afterwards, the TCP (4800 mg) and GO (16 mg) were added to the CH/Gel solution. Then, this solution was homogenized for 30 min by using an X10/25 Ultra-turrax. Subsequently, the TCP/Gel/CH/GO solution was loaded into a syringe (10cc Luer Lock) and extruded by a Fab@Home 3D printer.

After the printing process, each scaffold (n=9) was treated with LAA (10 mM; 6 mL) at 40 ˚C for 24 h (30 rpm) - *in situ* green reduction. Subsequently, the scaffolds were crosslinked through their immersion in a sodium tripolyphosphate (TPP) solution (10% (w/v)) for 48 h and air-dried at RT overnight, yielding TGC_irGO scaffolds.

For comparative purposes, TGC_GO and TGC scaffolds were also produced. The TGC_GO scaffolds were produced following the above described protocol but were not subjected to the *in situ* reduction method. In turn, the TGC scaffolds were also produced as described above but did not incorporate GO and were not subjected to the *in situ* reduction process.

### 2.2.3. Characterization of the morphology of the 3D scaffolds

The morphology and surface features of the scaffolds were evaluated through Scanning Electron Microscopy (SEM) analysis. For this purpose, samples were mounted onto aluminium stubs with araldite glue and then coated with gold using a Quorum Q150RES sputter coater (Quorum Technologies, UK). SEM images were acquired at different levels of magnification, at an acceleration voltage of 20 kV, using a Hitachi S-3400N scanning electron microscope (Japan).

### 2.2.4. Characterization of the physico-chemical properties of the scaffolds

#### 2.2.4.1. ATR-FTIR and EDS analysis

The physico-chemical composition of the scaffolds was evaluated by ATR-FTIR as described in section 2.2.1. [139]. All scaffolds were crushed to powder prior to the analysis. For comparison purposes, the scaffolds' components were also analysed in their pure state. On the other side, EDS was used to assess the elemental composition of the different scaffolds as described in section 2.2.1..

### 2.2.5. Characterization of the mechanical properties of the scaffolds

The mechanical behaviour of the scaffolds (n=5) was studied in dry and wet conditions, to mimic the physiological environment found in *in vivo* conditions. The wet scaffolds were attained through their immersion in a standard simulated body fluid (SBF) solution during overnight. The SBF solution was prepared according to a method previously described in literature, presenting an ion concentration similar to that existing in human blood plasma (142.0 mM $Na^+$, 5 mM $K^+$, 1.5 mM Mg2$^+$, 2.5 mM $Ca^{2+,}$ 147.8 mM $Cl^-$, 4.2 mM $HCO_3^-$, 1.0 mM $HPO_4^{2-}$ and 0.5 mM $SO_4^{2-}$) and a pH of 7.4 [140].

For the evaluation of the mechanical properties of the scaffolds, the 3D structures were subjected to compressive assays, as previously described by Torres *et al.* [141]. The measurements were performed at RT using a Shimadzu AG-X Tensile Testing Machine (Tokyo, Japan) with a crosshead speed of 3 mm/min and a load cell of 5 kN. The compressive strength ($C_s$) was determined using Equation (1):

$$C_S = \frac{F}{w \times l} \qquad (1)$$

Where F corresponds to the load at the time of fracture, w and l represent the width and length of the scaffolds, respectively.

The Young Modulus (YM) was determined by the stress-strain relation, using Equation (2) [141]:

$$YM = \frac{C_S}{H_d} \qquad (2)$$

Where $C_s$ is the scaffold compressive strength and $H_d$ represents the height deformation at maximum load.

### 2.2.6. Characterization of the swelling profile of the scaffolds

The swelling capacity of the scaffolds was determined through a method adapted from the literature [142]. Briefly, the scaffolds (n=5) were immersed in phosphate buffered saline (PBS) solution, at 37 °C, during 12 h under stirring (60 rpm). At predetermined intervals, scaffolds were withdrawn from the solution and weighted. After this process, the samples were re-immersed in the swelling solution. The swelling ratio was determined using the Equation (3):

$$Swelling\ Ratio\ (\%) = \left(\frac{W_t - W_0}{W_0}\right) \times 100 \qquad (3)$$

Where $W_t$ and $W_0$ represent the final and initial weight of scaffolds, respectively.

### 2.2.7. Contact angle measurements

The contact angles were measured, using an OCAH 200 Contact Angle System (DataPhysics Instruments, Germany), operated in static mode at RT (water was used as the reference fluid). For each sample, water drops were placed at various locations at the surface of the scaffold [93]. The reported contact angles are the average of at least five measurements.

### 2.2.8. Evaluation of scaffolds' porosity

The total porosity of the scaffolds was determined through the liquid displacement method, according to a protocol described in the literature [141]. The scaffolds were weighted and immersed in an absolute ethanol solution (EtOH) for 48 h. Subsequently, the scaffolds were weighted again. EtOH was used due to its capacity to penetrate inside the scaffold structure, without eliciting swelling, shrinkage and structural changes. The scaffolds' porosity was calculated by the amount of EtOH absorbed according to Equation (4) [143]:

$$Porosity\ (\%) = \frac{W_w - W_d}{D_{EtOH} - V_{scaffold}} \times 100 \qquad (4)$$

Where $W_w$ and $W_d$ refer to the wet and dry weights of the scaffolds, respectively. $D_{EtOH}$ represents the density of EtOH at RT and $V_{scaffold}$ is the volume of the wet scaffold.

### 2.2.9. Analysis of the enzymatic biodegradation profile of the scaffolds

The degradation profile of the scaffolds was evaluated by incubating them in PBS containing 13.6 mg/L of lysozyme, at 37 ˚C under stirring (60 rpm), over a period of 21 days. All the experiments were conducted in triplicate and the solutions were changed periodically in order to guarantee that the enzyme remained active through the study [144].

At predetermined timepoints, samples were removed from the solution and weighted, after being completely dry. The weight loss percentage at each timepoint was calculated according to Equation (5):

$$Weight\ loss\ (\%) = \left(\frac{W_i - W_f}{W_i}\right) \times 100 \qquad (5)$$

Where $W_i$ represents the initial weight of the scaffold and $W_f$ the weight of the scaffold at time t.

### 2.2.10. *In vitro* biomineralization assay

The *in vitro* bioactivity of the scaffolds was evaluated by incubating them an SBF solution (prepared as described in Section 2.2.5.) at 37 ˚C for 1, 3, 7, 14 and 21 days [140]. After each period of incubation, the scaffolds were removed and dried to visualize the apatite layers and quantify the deposition of calcium and phosphate ions on the scaffolds' surface by SEM and EDS analysis, respectively.

### 2.2.11. Characterization of the biological properties of the scaffolds

#### 2.2.11.1. Evaluation of cell viability and proliferation in contact with the scaffolds

The cytotoxic profile of the scaffolds towards normal human osteoblast (hOB) cells was evaluated through the MTS assay [121]. In brief, different scaffolds' formulations were cut into small pieces, placed into 96-well plates and then sterilized under UV radiation for 1 h. Subsequently, hOB cells were seeded in contact with the scaffolds at a density of $10 \times 10^3$ cells/well. After 1, 3 and 7 days of incubation, the medium was removed and cells were incubated with 120 μL of fresh medium containing MTS (20 μL) for 4 h (37 ˚C, 5% $CO_2$). Then, the absorbance of the samples was measured at 490 nm, using a microplate reader (Bio-Rad xMark microplate spectrophotometer). Cells incubated without the materials were used as the negative control ($K^-$), while cells incubated with EtOH (70%) were used as the positive control ($K^+$).

### 2.2.11.2. Characterization of cell adhesion at the surface of the scaffolds

Cell adhesion at the surface of the scaffolds was evaluated by SEM. In brief, hOB cells were seeded (40 x $10^3$ cells/wells) in contact with the scaffolds. After 1, 3 and 7 days of incubation, the samples were washed and fixed with glutaraldehyde (2.5% (v/v)) for 30 min. Then, the samples were frozen at -80 ˚C, freeze-dried for 3 h and prepared for SEM analysis (as described in the section 2.2.3.).

### 2.2.11.3. Confocal microscopic analysis

The cell distribution within the scaffolds was characterized by using confocal laser scanning microscopy (CLSM). In brief, hOB cells (20 x $10^3$ cells/scaffold) were seeded in the presence of scaffolds in µ-Slide 8-well Ibidi imaging plates (Ibidi GmbH, Germany) [18]. After 72 h, the samples were treated with a permeabilization solution (Triton X-100) and the cell nucleus was labelled with propidium iodide (PI; 15 mM) during 15 min at 37 ˚C. Then, the samples were washed with PBS and fixed with 4% paraformaldehyde (PFA), for 15 min, at RT. Imaging experiments were then performed in a Zeiss LSM 710 laser scanning confocal microscope (Carl Zeiss SMT Inc., USA), where consecutive z-stacks were acquired. 3D reconstruction and image analysis were performed in Zeiss Zen 2010 [19].

### 2.2.11.4. Alizarin Red S (ARS) staining

The capacity of scaffolds to promote calcium deposition by hOB cells was evaluated by an ARS staining method, following a protocol previously optimized by our group [121]. Briefly, cells were seeded (10 x $10^2$ cells/well) in contact with the scaffolds (n=6) in 6-well plates. After 1, 3, 7, 14 and 21 days of incubation, the samples were fixed with formaldehyde (4% (v/v)) during 1 h. Afterwards, samples were stained with 1 mL of ARS (40 mM, pH= 4.1 - 4.3) during 1 h, under gentle shaking. Subsequently, the samples were washed twice with deionized $H_2O$ to remove the excess of ARS. Then, microscopic images were acquired to visualize the calcium deposits produced by hOB cells at the surface of the scaffolds.

Subsequently, the ARS adsorbed on scaffolds was quantified by eluting it with acetic acid (1 mL; 10% (v/v)) under shaking for 30 min. Thereupon, the samples were vortexed for 30 s and the liquid phase was heated at 85 ˚C for 10 min. Afterwards, the samples were centrifuged (14 000 g, 25 min, RT), followed by neutralization of the supernatant (500 µL) with ammonium hydroxide (200 µL; 10% (v/v)). Finally, the absorbance was measured at 405 nm using a microplate reader (Biorad xMark microplate spectrophotometer). The ARS concentration was then determined using a standard curve.

### 2.2.11.5. Alkaline Phosphatase (ALP) activity and dsDNA quantification

The ALP activity of hOB cultured in contact with 3D scaffolds was evaluated as described elsewhere [145]. Briefly, hOB cells were cultured in the presence of the scaffolds during 1, 3, 7, 14 and 21 days (as described in section 2.2.11.1). Afterwards, samples were treated with Triton X-100 (1 mL) and a cell scraper was used to remove the cell-scaffolds constructs, which were then transferred into eppendorfs. Thereafter, the samples were subjected to a freeze-thaw cycle and sonicated for 15 min to promote cells' lysis. Afterwards, the samples were centrifuged (14 000 g, 15 min, at RT) and the supernatant was collected to quantify the ALP activity and the dsDNA content.

The ALP activity was determined by incubating the samples' supernatant (20 µL) with 60 µL of a substrate solution (0.2% *p*-Nitrophenylphosphate (pNPP) (w/v) in 1 M diethanolamine HCl, at pH 9.8) for 45 min at 37 °C in the dark. Subsequently, 80 µL of the stop solution (NaOH (2 M) containing EDTA (0.2 mM)) was added. Then, the production of *p*-nitrophenol was evaluated by measuring the absorbance at 405 nm. The ALP activity was determined according to the protocol provided by the manufacturer.

The total DNA content was quantified using the Quant-iT PicoGreen Kit (Invitrogen, Carlsbad, CA) as recommended by the manufacturer. Briefly, 100 µL of the PicoGreen reagent (1:200 dilution of the PicoGreen reagent in 1X TE Buffer) was incubated with an equal volume of the cell's lysate for 5 min in the dark. Afterwards, the fluorescence was measured in a microplate reader using an excitation and emission wavelengths of 485 and 535 nm, respectively. Samples' dsDNA content was then determined by using a standard curve.

## 2.2.12. Evaluation of the bactericidal activity of the scaffolds

*S. aureus* and *E. coli*, gram-positive and gram-negative bacteria, were used to characterize the antibacterial activity of the scaffolds. For this purpose, a modified Kirby-Bauer technique was used [139]. Briefly, 200 µL of the bacteria medium (at a concentration of 1 x $10^8$ CFU/mL) were dispensed onto an agar plate. Circular scaffolds (n=3) were then placed on the agar plate and incubated during 24 h at 37 °C. Afterwards, the inhibitory halos around the samples were photographed and their diameters were measured using the *ImageJ* software. The bacteria growth at surface of the scaffolds was also confirmed by SEM analysis (samples were prepared as described in section 2.2.3.).

### 2.2.13. Statistical analysis

One-way analysis of variance (ANOVA) with the Newman-Keuls post hoc test was used for the analysis of the obtained results. A $p$ value lower than 0.05 ($p < 0.05$) was considered statistically significant.

# Chapter III

# 3. Results and Discussion

## 3.1. Characterization of GO and rGO produced by direct reduction with LAA

The DLS analysis confirmed that after sonication the GO samples display a nanometric size distribution (Figure 11 A). The FTIR characterization revealed that the GO presents peaks at 3331, 2921, 1713, 1635, and 1073 cm$^{-1}$ belonging to the O-H, C-H, C=C, C=O and C-O stretches, respectively (Figure 11 B). Furthermore, EDS characterization demonstrated that GO has a C:O ratio of 66:34 (Table 1). These results are in agreement with the data available in literature [121]. As a control, rGO obtained by the direct reduction with LAA was also produced. The FTIR spectrum of this material displayed the peaks of the oxygen-functional groups with a decreased intensity, which is also demonstrated in EDS results (C:O ratio of 80:20 (Table 1)). Such results confirm that by treating GO with LAA, for 24 h, at 40 ºC, induces its reduction. However, the rGO attained by the direct reduction with LAA formed visible aggregates (Figure 11 C), which hinder its incorporation in blends aimed to be used in the printing of the 3D scaffolds.

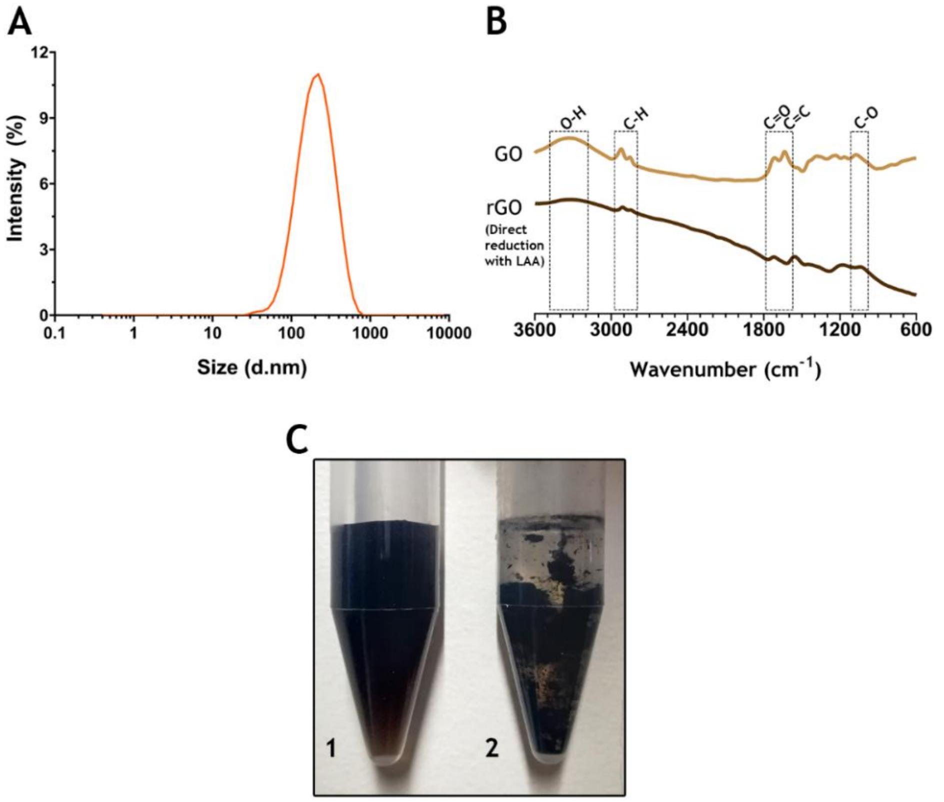

**Figure 11**. Characterization of physico-chemical properties of GO and rGO. DLS characterization of GO (A); ATR-FTIR analysis of GO and rGO (direct reduction with LAA) powders (B); images of as-prepared GO (C1) and rGO obtained by direct reduction with LAA (C2) solutions.

**Table 1.** EDS analysis of GO and rGO produced by direct reduction of GO with LAA.

| | **Elements ($^a$at.%)** | |
|---|---|---|
| **Sample** | C | O |
| GO | 66.36 | 33.64 |
| rGO (direct reduction with LAA) | 80.37 | 19.63 |

$^a$at.%—atomic percentage

## 3.2. Morphological characterization of the scaffolds

The fabrication process used to produce the TGC_irGO scaffolds is schematically represented in Figure 12 A. First, a homogeneous mixture of TCP, Gel, CH and GO was deposited layer-by-layer, resulting in the formation of the 3D scaffolds that mimic the natural bone matrix composition (20-30% organic, 70-80% inorganic) [95, 139]. In this case, TCP confers mechanical and osteogenic properties to the scaffolds [146]. On the other hand, Gel and CH provide bioadhesive and antibacterial properties, respectively. Then, the environmentally-friendly *in situ* reduction of the GO incorporated within the scaffolds is performed by immersing the 3D matrices in a solution containing LAA, for 24 h, at 40 °C. By employing this novel approach, it was possible to overcome the problems associated with the inclusion of rGO in 3D printed scaffolds. Furthermore, this temperature and incubation period were selected to ensure the integrity of the produced scaffolds as well as to grant an appropriate reduction of the GO. Finally, the obtained materials were crosslinked and air-dried, yielding TGC_irGO scaffolds. To fully disclose the possible improved bone healing properties of TGC_irGO scaffolds resulting from the presence of rGO, TGC_GO scaffolds (incorporate GO but that was not subjected to the *in situ* reduction) and TGC scaffolds (without containing GO and without being subjected to a reduction process) were also prepared.

The suitability of the *in situ* green reduction of the GO incorporated on TGC scaffolds was then analysed. The TGC_irGO scaffolds displayed a similar design and shape to that of both TGC_GO and TGC scaffolds (Figure 12 B). These results indicate that the *in situ* green reduction process is not detrimental for the macroscopic structure of the scaffolds. However, the TGC_GO scaffolds presented a dark brown colour, due to the original GO solution colour (Figure 11 C) [121]. Furthermore, the *in situ* green reduction process produced a darker TGC_irGO scaffolds (Figure 12 A). Such phenomenon is attributed to the *in situ* formation of rGO, which has a dark black colour [147, 148]. As a control, the direct reduction of GO with LAA was also performed (Figure 11 C). The rGO formed in these conditions aggregated during the reduction process, which did not allow its printability (Figure 11 C). These results further confirm suitability of the *in situ* green reduction process for attaining 3D printed scaffolds incorporating rGO.

Then, the surface' morphology of the scaffolds was characterized through the acquisition of SEM images. The TGC, TGC_GO and TGC_irGO scaffolds presented a similar architecture and macroporosity, showing high roughness on their surface (Figure 12 C and 15), which is an essential feature for cells' adhesion [74]. Kanayama *et al.* reported that collagen films coated with rGO display an increased nanoscale roughness in comparison to their equivalents coated with GO [132]. Such results suggest that TGC_irGO scaffolds may provide additional anchorage points for cell attachment and proliferation.

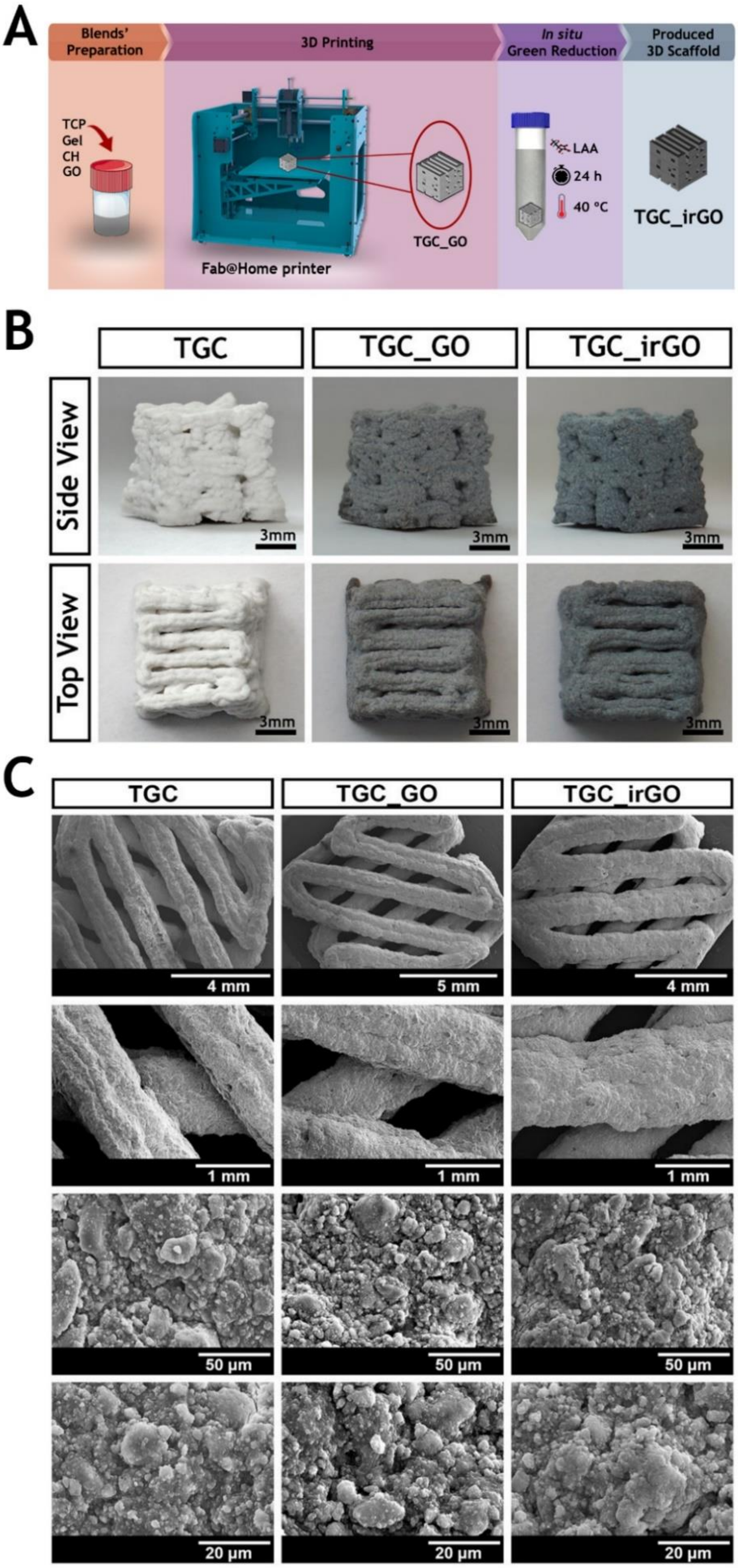
A
Blends' Preparation
3D Printing
In situ Green Reduction
Produced 3D Scaffold
TCP
Gel
CH
GO
Fab@Home printer
TGC_GO
LAA
24 h
40 °C
TGC_irGO
B
TGC
TGC_GO
TGC_irGO
Side View
Top View
3mm
C
TGC
TGC_GO
TGC_irGO
4 mm
5 mm
4 mm
1 mm
50 µm
20 µm

**Figure 12.** Production and characterization of 3D scaffolds. Schematic representation of experimental setup used to produce the TGC_irGO scaffolds production (A); representative macroscopic images of the different scaffolds produced (side and top views) (B) and SEM images showing the morphology and surface topography of the 3D scaffolds produced at different magnifications (C).

## 3.3. Characterization of the physico-chemical properties of the produced scaffolds

The chemical composition of the produced scaffolds was then characterized by FITR analysis. The spectra of the powdered scaffolds revealed the characteristic peaks of the chemical bonds present on TCP (P=O stretch at 1200 cm$^{-1}$) and on both Gel and CH (O-H, C-H, C=O N-H (I) and (II) stretches at 3292, 2871, 1640, 1530 and 3284 cm$^{-1}$, respectively) (Figure 13 A and B). The peaks of the chemical groups present on GO and rGO overlap those of the other materials present on TGC_GO and TGC_irGO scaffolds, respectively (Figure 11B and 13 B). Thus, an EDS analysis was also performed to characterize the scaffolds' composition (Table 2). Compared to the TGC scaffolds, the TGC_GO scaffolds demonstrated a higher content of carbon and a lower amount of oxygen elements (Table 2). These results corroborate the presence of GO on the TGC_GO scaffolds since this nanomaterial has a high C:O ratio of 66:34 (Table 1). Furthermore, the TGC_irGO scaffolds presented the highest and lowest content of carbon and oxygen, respectively. These results further confirm the presence of rGO in the TGC_irGO scaffolds since the former has a C:O of 80:20 (as determined by the direct reduction of GO with LAA) (Table 1). Moreover, these observations also validate the reduction capacity of the *in situ* method herein developed. As importantly, TGC_irGO and TGC_GO scaffolds presented a higher content of phosphorus and calcium when compared to the TGC scaffolds (Table 2). Such results indicate that these formulations may display an improved mineralization capacity. In fact, graphene-based materials' larger surface area and rough surface can promote the adsorption of biomolecules and ions (like calcium), and consequently improve the osteoinductivity and osteoconductivity of the 3D scaffolds [149, 150]. The small content of sodium detected on scaffolds is related to the use of TPP as the crosslinking agent (Table 2).

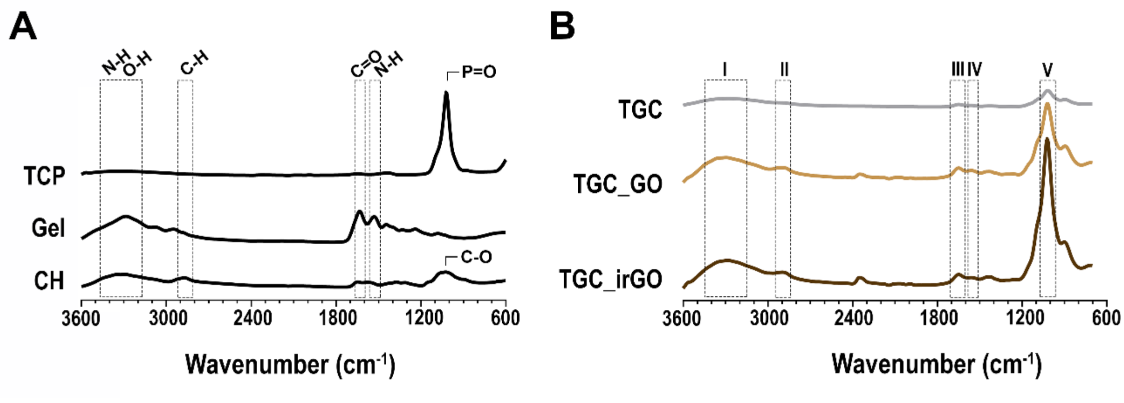

**Figure 13**. ATR-FTIR analysis of TCP, Gel, CH (A) and TGC, TGC_GO, TGC_irGO scaffolds (B). I: O-H and N-H (I) stretches; II: C-H stretch; III: C=O stretch; IV: N-H (II) stretch; V: P=O and C-O stretches.

**Table 2**. EDS analysis of the 3D printed scaffolds.

| | **Elements ([a]at.%)** | | | | |
|---|---|---|---|---|---|
| **Sample** | C | O | Na | P | Ca |
| TGC | 16.85 | 51.62 | 2.45 | 11.54 | 17.54 |
| TGC_GO | 17.71 | 44.24 | 2.76 | 14.50 | 20.79 |
| TGC_irGO | 19.75 | 41.56 | 3.76 | 15.49 | 19.44 |

[a]at.% — atomic percentage

## 3.4. Characterization of the mechanical properties of the scaffolds

After confirming the successful preparation of TGC_irGO scaffolds, the mechanical properties of this 3D structure were compared to those of TGC_GO and TGC scaffolds. This is of paramount importance since the mechanical properties are crucial for scaffolds' maintain, replace or improve the bone tissue functions [71, 77]. Furthermore, scaffolds' mechanical properties should be as close as possible to the native tissue. Such is crucial to avoid problems like osteopenia due to the use of bone grafts that are stiffer than the original bones or trigger the occurrence new fractures due to low mechanical strength [151].

Therefore, the compressive strength ($C_s$) and Young modulus (YM) of the 3D scaffolds were determined through a compression assay performed at dry and wet states (Figure 14). In dry conditions, scaffolds presented high $C_s$ values (Figure 14 A). Furthermore, TGC_irGO scaffolds presented a higher $C_s$ value than TGC_GO and TGC scaffolds. This reinforcement on the mechanical properties of the TGC_irGO scaffolds can be explained by the presence of rGO on this material. In fact, the incorporation of rGO on matrices has been shown to improve their mechanical properties to a greater extent than GO [132]. Together these results confirm that the *in situ* green reduction method used herein can be explored to improve the mechanical properties of scaffolds incorporating GO. At the wet state, the $C_s$ values decreased for all the 3D printed formulations (Figure 14 A). In this condition, the scaffolds present $C_s$ values within the range displayed by the trabecular bone (2-20 MPa) [71].

Furthermore, the scaffolds displayed more elasticity (lower YM values) than that found in the native bone (100-2000 MPa; Figure 14 B). However, the produced scaffolds are designed to act as templates during the first phases of the bone regeneration, suffering biodegradation and replacement by the newly formed bone matrix. Such features allow scaffolds to confer a temporary support, accelerate the regeneration process, and improve the mechanical stability of the fracture site during the mineralization phase [152, 153].

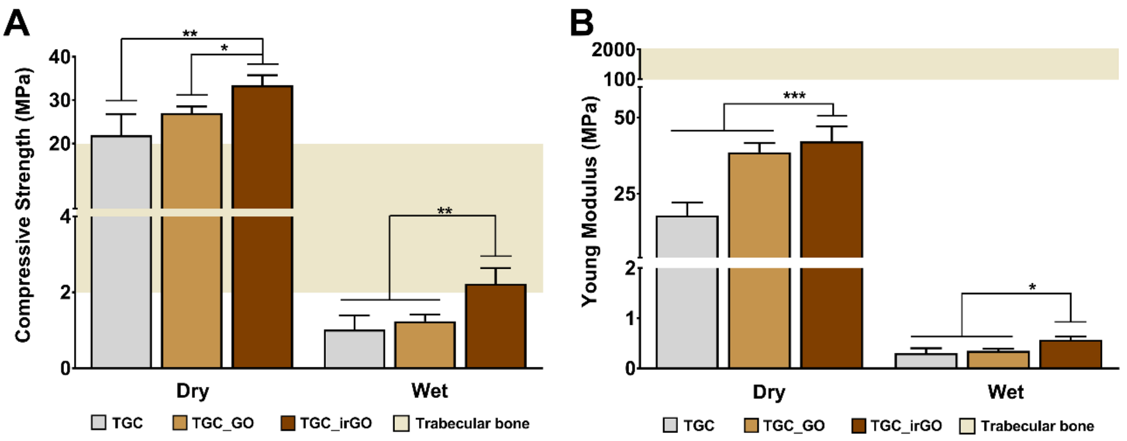

**Figure 14.** Characterization of the $C_S$ (A) and YM (B) of the produced 3D scaffolds under dry and wet conditions (data represent the mean ± standard deviation, n = 5, $^{*}p < 0.05$, $^{**}p < 0.01$ and $^{***}p < 0.001$).

## 3.5. Evaluation of the swelling profile of the produced scaffolds

Scaffolds' swelling capacity is essential for their application in bone regeneration. This absorption of fluids will promote the expansion of the polymeric matrix, leading to an increase on the scaffolds' pore size, which in turn facilitates cellular internalization processes and the diffusion of nutrients and waste along the scaffolds' structure. However, a continuous swelling must be avoided since this may induce loss of the scaffolds' mechanical integrity and can induce compressive stress to the surrounding tissue, causing pain to the patient [154].

The swelling behaviour of the 3D printed scaffolds was then investigated through their incubation in PBS during 12 h (Figure 16 A). The three formulations exhibited a similar behaviour, characterized by an abrupt swelling in the first 2 h, followed by a plateau phase (Figure 16 A). This behaviour is explained by the presence of hydrophilic groups (amine and hydroxyl) on the CH and Gel backbones than can be easily hydrated. Moreover, the swelling of CH involves the protonation of amine groups and mechanical relaxation of the coiled CH chains [155]. This swelling behaviour is in agreement with that of other 3D printed scaffolds prepared using polymeric materials and TCP reported in the literature [121, 156].

## 3.6. Determination of the wettability of the surface of the produced 3D scaffolds

The scaffolds' surface wettability is another surface property that may influence the biological response of implanted materials, affecting the protein adsorption and cell adhesion [157, 158]. Scaffolds' surface wettability can be assessed through the measurement of water contact angles (WCA) [93]. In the literature, it is reported that cell adhesion is more favoured on surfaces displaying a moderate hydrophilic character (40˚< WCA < 70˚) than on hydrophobic (WCA > 90˚) or super hydrophilic surfaces (WCA < 20˚) [159, 160].

The results revealed that TGC scaffolds exhibit a WCA value of ≈ 20˚, demonstrating a super hydrophilic character. Such value is attributed to the presence of hydrophilic groups on CH and Gel backbones (Figure 16 B). However, highly hydrophilic surfaces limit or completely impair cellular attachment and spreading. In fact, cell adhesion mediating molecules bind weakly to super hydrophilic surfaces [159, 161]. The TGC_GO scaffolds presented a WCA of ≈ 30˚, which can be explained by the presence of GO on this matrix. In contrast, the TGC_irGO scaffolds displayed a WCA of ≈ 42˚, which is in agreement with the presence of rGO that has a hydrophobic character. This finding indicates that TGC_irGO scaffolds present a moderate hydrophilic character, which is considered to be optimal for promoting cell adhesion and proliferation.

## 3.7. Evaluation of scaffolds' porosity

Scaffolds' porosity has a remarkable effect on cells' infiltration, proliferation and growth. Moreover, the interconnected pores can facilitate the diffusion of $Ca^{2+}$ and $PO_4^{3-}$ ions throughout the scaffolds, allowing the formation of a hydroxyapatite-like layer that stimulates osteoblasts' cellular activity and the deposition of bone matrix [162].

A liquid displacement method was employed to analyse the total porosity of the scaffolds (Figure 16 C). The 3D structures displayed a total porosity of 20 – 30% (Figure 16 C). Even though the scaffolds' total porosity is not ideal when compared to that presented by the trabecular bone (50 – 90%) [163]. However, the ability of 3D structures to support cells' infiltration is not solely dependent on this feature. In fact, Boga *et al.* produced 3D printed scaffolds containing GO that displayed a total porosity of about 35%, that were able to support cells' infiltration, adhesion and proliferation [121]. Furthermore, highly porous scaffolds possess a low density and thus may have a lower mechanical strength [78, 164]. On the other hand, SEM analysis revealed that scaffolds present a suitable macroporosity by displaying macropores with 1600-1900 μm of diameter (Figure 15). Such values of porosity are close to the pore diameter range that is considered to be optimal for promoting cells' infiltration, new vessels' ingrowth as well as for promoting an adequate exchange of nutrients and oxygen [165].

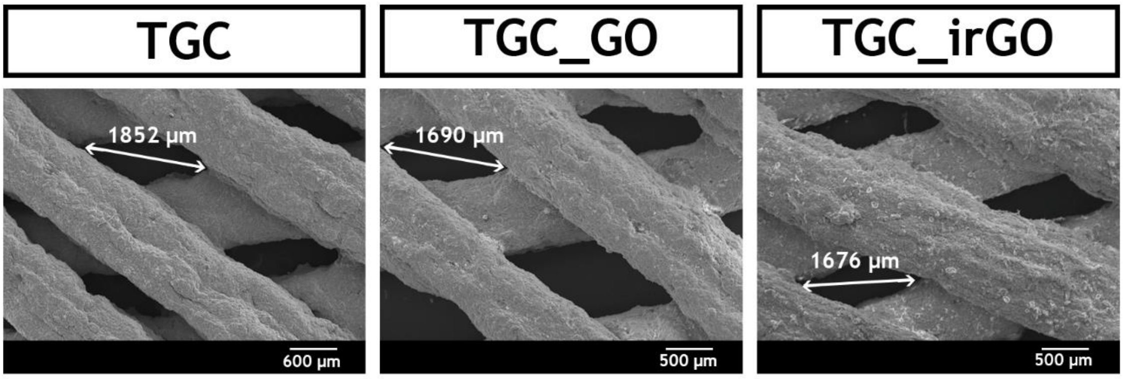

**Figure 15.** SEM images that characterize the pore diameters on scaffolds' surfaces.

## 3.8. Characterization of enzymatic degradation profile of the scaffolds

The biodegradation profile of the scaffolds is a crucial factor for their long-term application in bone regeneration. In this regard, scaffolds' degradation rate must be proportional to the new bone formation rate, without compromising the stability of the construct nor the integrity of the tissue at the injured site [73].

The degradation profile of the produced scaffolds in PBS containing lysozyme (an enzyme found in human serum) was then studied (Figure 16 D). Lysozyme mediates the hydrolyzation of the N-acetyl glucosamine groups of CH [144]. In turn, the macromolecular chains of the Gel are then easily hydrolysed in the presence of water, due to their hydrophilic character [166]. The TCP suffers degradation mediated by cells and its products are naturally metabolized during the resorption bone process [156].

During the first days of incubation, all the scaffolds suffered an initial weight loss (Figure 16 D), a phenomenon that was slightly more pronounced for the TGC_irGO scaffolds. The TGC_irGO scaffolds' earlier degradation can be correlated to its possible higher surface roughness, which may increase their interactions with the surrounding medium, triggering a faster weight loss. Nevertheless, TGC_irGO scaffolds degradation progressively stabilized to the values observed for TGC and TGC_GO scaffolds. Moreover, none of the scaffolds' formulations lost more than 25% of their initial weight, over a period of 21 days, indicating their suitability to be applied in bone regeneration applications.

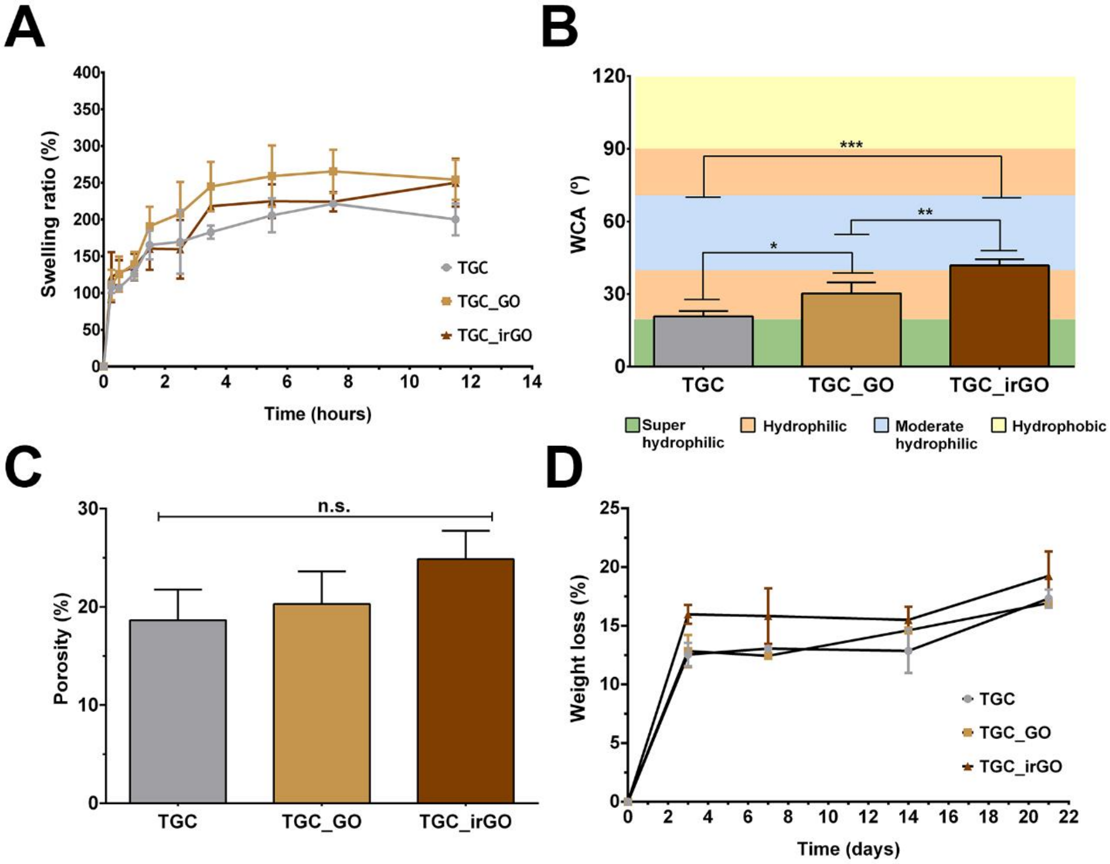

**Figure 16**. Characterization of physico-chemical properties of the produced scaffolds. Characterization of scaffolds' swelling profile (A); evaluation of the scaffolds' surface wettability by measuring the water contact angles (WCA) (B); evaluation of scaffolds' total porosity (C); determination of scaffolds' weight loss over time (D) (data represent the mean ± standard deviation, n = 5, $^*p < 0.05$, $^{**}p < 0.01$ and $^{***}p < 0.001$; the groups assigned with n.s. were not statistically significant).

## 3.9. *In vitro* biomineralization assay

The ability of scaffolds' surface to promote the deposition of minerals was also studied. Such property is related with the fixation of the phosphate and calcium ions in the form of hydroxyapatite crystals ($Ca_5(PO_4)_3(OH)$), which is crucial for bone regeneration [167].

Thus, scaffolds' biomineralization over a period of 21 days in SBF was characterized (Figure 17). For this purpose, the formation of apatite crystals on the scaffolds' surface was visualized through SEM analysis (Figure 17 A). EDS characterization was also performed to quantify the calcium and phosphate ions on scaffolds' surface (Figure 17 B and 17 C). The obtained results revealed that all scaffolds' formulations promoted the deposition of calcium and phosphate over time. These results can be justified by the intrinsic ability of TCP to induce the mineralization at the surface of the scaffolds, increasing their biointegration and, hence the bone regeneration process [166, 168].

The extensive physico-chemical characterization performed in this study revealed that the TGC_irGO scaffolds present an improved wettability and mechanical properties when compared to the TGC_GO and TGC scaffolds. Moreover, all scaffold formulations displayed a suitable porosity and swelling behaviour as well as adequate rates of minerals' deposition and degradation rate.

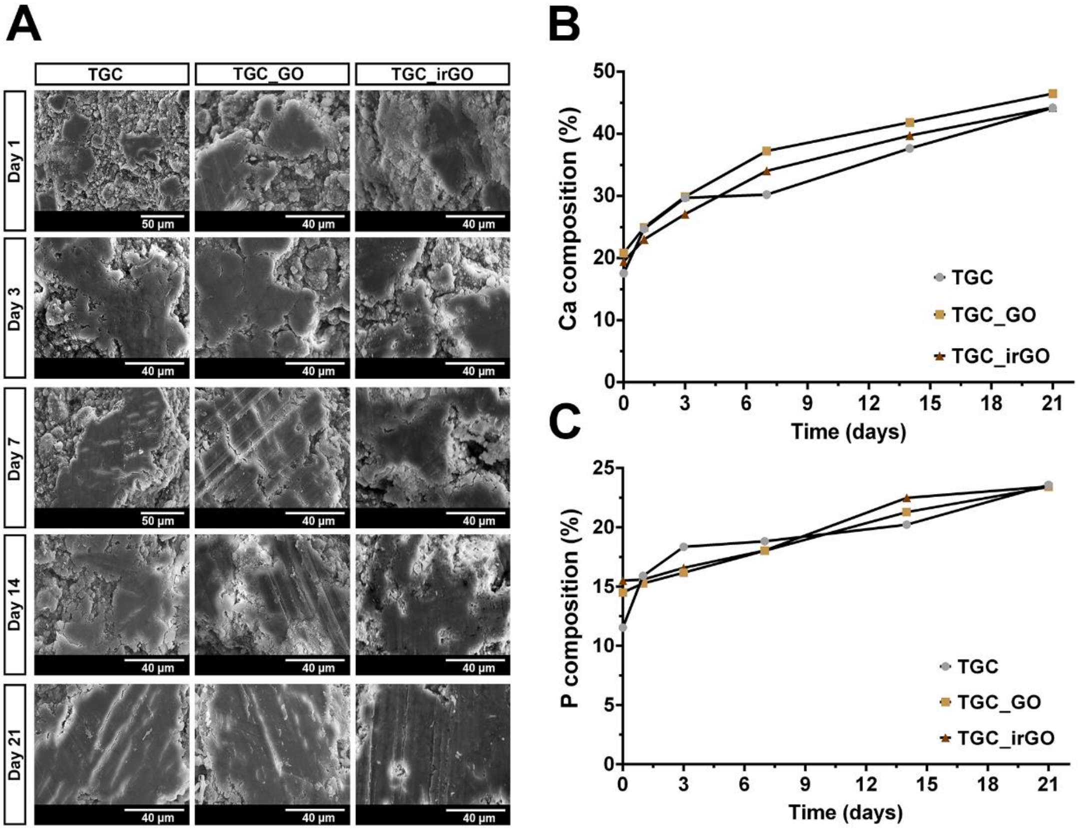

**Figure 17**. Evaluation of the biomineralization at the surface of the produced scaffolds in contact with SBF. SEM images of the scaffolds' surface showing the mineral deposition at scaffolds' surface, after their incubation in SBF solution for 1, 3, 7, 14 and 21 days (A); EDS analysis of calcium (B) and phosphorous atomic percentages (C) on scaffolds' surfaces.

## 3.10. Characterization of the biological properties of the produced scaffolds

### 3.10.1. Evaluation of scaffolds' cytotoxic profile

To characterize the cytotoxic profile of the produced scaffolds and their degradation products, an MTS assay was performed [71]. For this purpose, scaffolds were placed in contact with hOB cells since these cells are involved in synthesis of bone tissue ECM and have an important role in the mineralization process [167].

The obtained results revealed that hOB cells remained viable when in contact with the scaffolds (Figure 19 A), even after 7 days of incubation. Furthermore, the optical microscopy images also demonstrate that hOB cells proliferated and exhibited an elongated and flattened morphology in contact with scaffolds (Figure 18). These results are in agreement with those previously reported by Serra *et al.*, who produced 3D sponges with the same ceramic/polymer mixture for being used in bone regeneration [169].

Moreover, TGC_irGO scaffolds' biocompatibility was similar to TGC and TGC_GO scaffolds (Figure 19 A). This is of paramount importance since the direct administration of rGO to cells has been shown to have a cytotoxic effect, which can be attributed to the low water solubility of this nanomaterial and also to the presence of hydrazine hydrate (a commonly used reducing agent) [170]. In this way, these results further confirm the potential of the *in situ* green reduction method developed herein to produce 3D printed scaffolds incorporating rGO with improved biocompatibility for bone regeneration applications.

Furthermore, hOB cells adhesion at scaffolds' surface was also analysed through the acquisition of the SEM images (Figure 19 B). Cells adhered and spread at the surface of the produced scaffolds. After 7 days, cells started to present the typical osteoblastic morphology, showing a smooth arrangement, and established connections between each other, forming a continuous cell layer. In this regard, the linear RGD-motifs of Gel may play an important role on cell adhesion [171]. As importantly, the number of hOB cells adhered on scaffolds' surface increased overtime (Figure 19 B), which further emphasizes the good biocompatibility of the produced scaffolds. Together, these results demonstrate that the 3D printed scaffolds display suitable properties for biological applications.

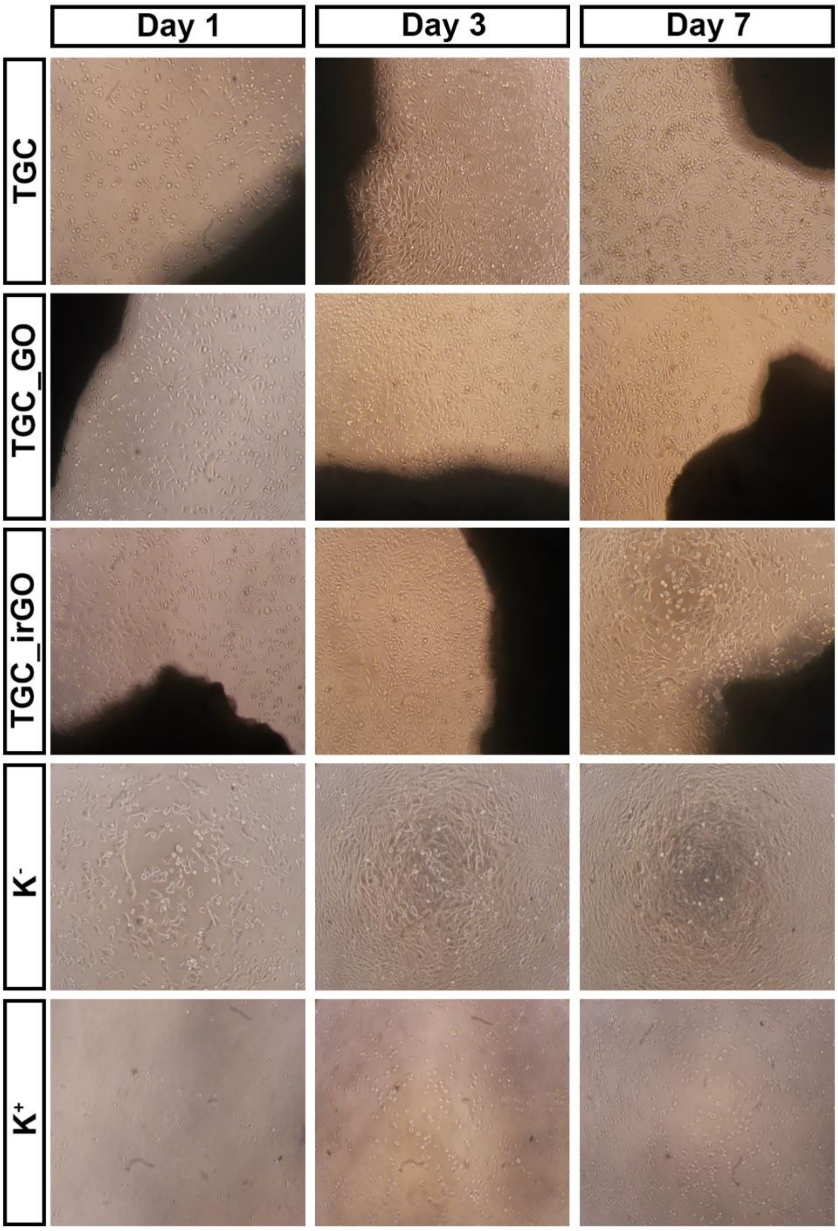
Day 1
Day 3
Day 7
TGC
TGC_GO
TGC_irGO
K-
K+

**Figure 18.** Optical microscopy images acquired to characterize cells' behaviour in contact with the produced scaffolds during 1, 3 and 7 days. Live and dead cells were used as negative ($K^-$) and positive ($K^+$) controls, respectively.

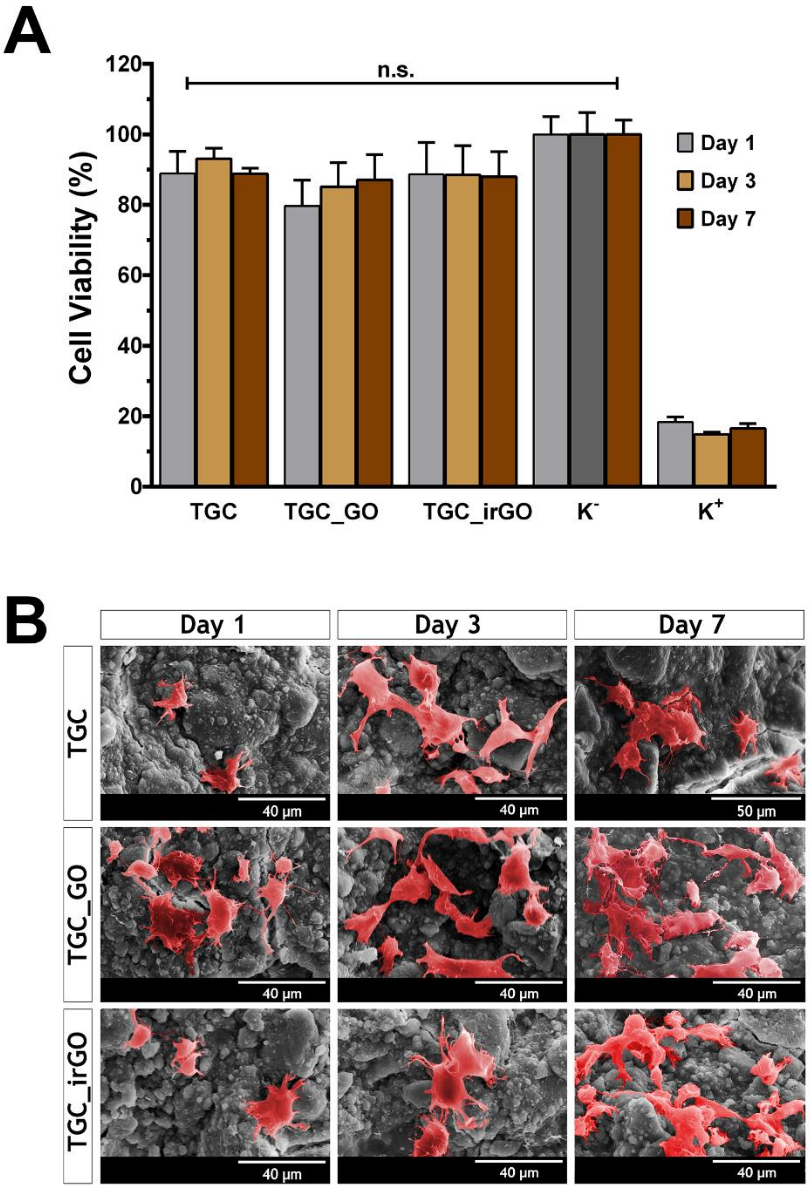

**Figure 19.** Characterization of the biological properties of the scaffolds. Evaluation of the cytotoxic profile of the produced 3D scaffolds through the MTS assays, at 1, 3 and 7 days. ($K^+$) positive control and ($K^-$) negative control were used for dead and viable cells, respectively (A) (each result is the mean ± standard deviation, n = 5; n.s: the groups assigned with n.s. were not statistically significant); Representative pseudo-colored SEM images of hOB cells seeded onto the surface of scaffolds over a period of 1, 3 and 7 days (B).

### 3.10.2. Confocal laser scanning microscopy (CLSM) analysis

The ability of cells to become internalized into the produced 3D printed scaffolds was also characterized (Figure 20). CLSM orthogonal projections revealed that hOB cells are able to migrate into the scaffolds' interior (Figure 20 D-F). Furthermore, the depth colour coding images also showed that the migration of hOB cells within the scaffolds' porous network (Figure 20 G-L) up to a depth of 60-100 μm (coloured in blue), with the majority of the cells remaining at the 20-40 µm depth (coloured in yellow). In this way, the produced 3D matrices have suitable properties to allow osteoblasts growth within their structure. Such is essential to improve cells' growth and differentiation, leading to an improved deposition of new bone matrix, and consequently bone tissue regeneration [172].

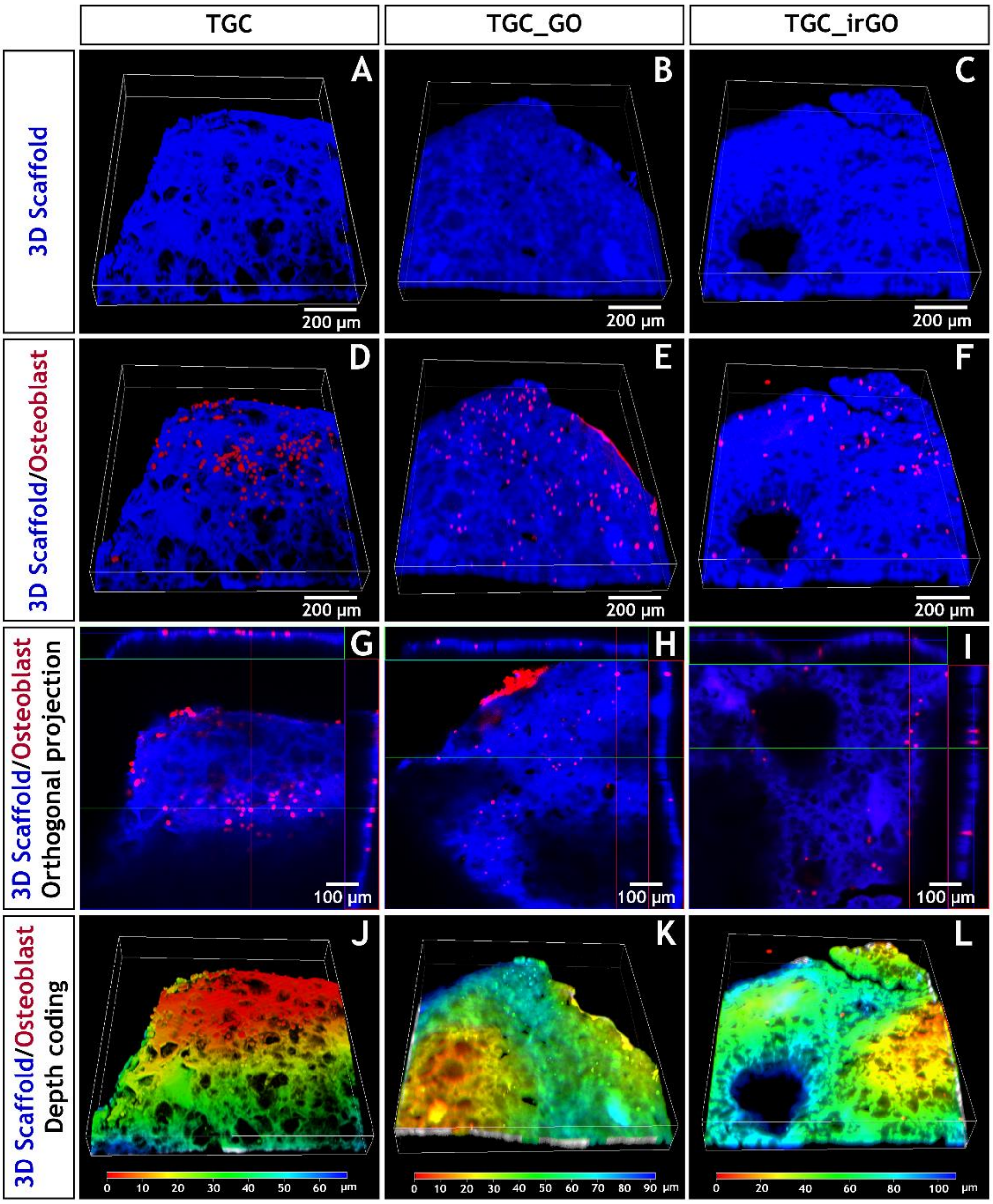
TGC
TGC_GO
TGC_irGO
3D Scaffold
3D Scaffold/Osteoblast
3D Scaffold/Osteoblast Orthogonal projection
3D Scaffold/Osteoblast Depth coding
A
B
C
D
E
F
G
H
I
J
K
L
200 µm
100 µm
0 10 20 30 40 50 60 µm
0 10 20 30 40 50 60 70 80 90 µm
0 20 40 60 80 100 µm

**Figure 20.** CLSM images acquired to characterize cell internalization within the TGC, TGC_GO and TGC_irGO scaffolds. 3D reconstruction images (A–F), orthogonal projections (G-I) of the cells in contact with scaffolds. Depth color coding CLSM images of the scaffolds are also presented (J-L).

### 3.10.3. Alizarin Red S (ARS) staining

The ARS staining was performed to evaluate the matrix mineralization activity performed by hOB cells in contact with the scaffolds [173]. For this purpose, optical microscopic images of the mineralized matrix were acquired after 1, 3, 7, 14 and 21 days of incubation (Figure 21 A), and the calcium deposits produced by the hOB cells were also quantified (Figure 21 B).

For all the scaffolds' formulations, the determined ARS concentration increased along time (Figure 21 B), revealing that the calcium deposition is promoted on all the scaffolds' surface. Particularly, TGC_irGO scaffolds presented a higher ARS concentration after 14 and 21 days of incubation, in comparison to TGC_GO and TGC scaffolds. The improved calcium deposition mediated by TGC_irGO scaffolds is in agreement with literature reports where the same behaviour was observed for matrices incorporating rGO [174, 175]. For example, Kanayama *et al.* reported that collagen films coated with rGO displayed a higher calcium adsorption than their equivalents containing GO [132]. The deposition of calcium at scaffolds' surface reflects their osteogenic property, which is important for BTE applications [176]. The results here obtained also disclosed that the *in situ* green reduction method can yield 3D printed scaffolds incorporating rGO with an enhanced biomineralization activity.

### 3.10.4. Determination of the Alkaline Phosphatase (ALP) activity

ALP is an important early osteogenic and biochemical marker of osteoblasts' differentiation [177]. Furthermore, the ALP is involved in the cleavage of organic phosphate, providing calcium and phosphate ions that are essential for the mineralization process of the bone matrix [178]. For this purpose, the ALP activity of hOB cells in contact with the 3D scaffolds (normalized to the DNA concentration) was measured along time (Figure 21 C).

Overall, hOB cells incubated with TGC_GO and TGC_irGO scaffolds presented a higher ALP activity than those incubated with the TGC scaffolds (Figure 21 C). After 14 days of incubation, cells in contact with TGC_GO or with TGC_irGO scaffolds displayed a 1.6 and 1.9-fold higher ALP activity, respectively, than those in contact with TGC scaffolds (Figure 21 C). These results are also in agreement with the ARS assays, in which the TGC_irGO scaffolds exhibited an improved calcium deposition. In fact, $Ca^{2+}$ can stimulate ALP activity and matrix mineralization [179].

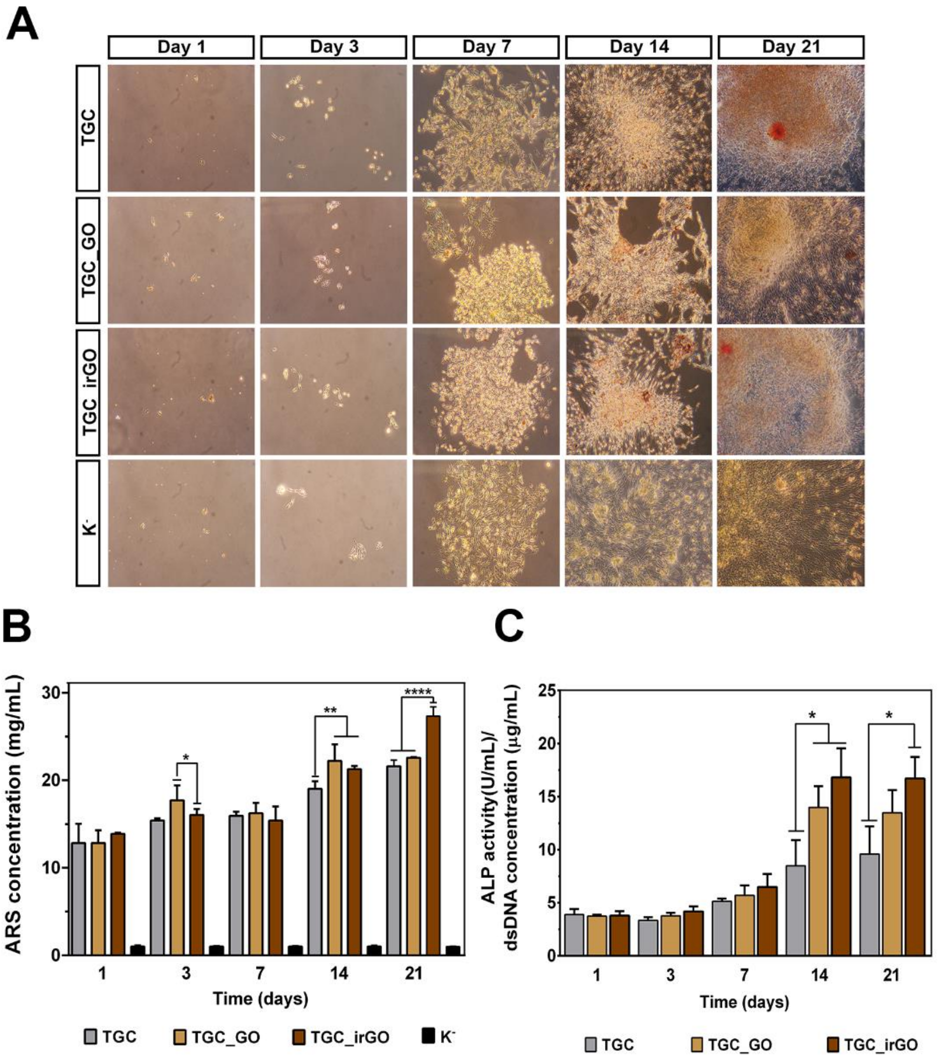

**Figure 21.** Characterization of the osteogenic properties of the produced scaffolds. Optical microscopy images of hOB cells stained with Alizarin Red S after 1, 3, 7, 14 and 21 days of incubation with TGC, TGC_GO and TGC_irGO scaffolds (A); Determination of the Alizarin Red concentration (B) and ALP activity (C) of hOB cells cultured in the presence of the 3D scaffolds after 1, 3, 7, 14 and 21 days of incubation (each result is the mean ± standard deviation, n=6, *p < 0.05, **p < 0.01 and ****p < 0.0001; the groups not signed with * were not statistically significant).

## 3.11. Evaluation of the bactericidal activity of the scaffolds

Bone implants failures are prompted by bacterial infections caused by microorganisms, that induce the formation of biofilms on implants' surface. These biofilms can compromise the successful application and function of the implants. Moreover, bacterial infections lead to prolonged hospitalization periods, increased costs, and in extreme cases, patient death [180].

Therefore, the antibacterial activity of the produced scaffolds against *S. aureus* and *E. coli* was screened through an agar diffusion method. The 3D printed scaffolds were able to inhibit the *S. aureus* and *E. coli* growth (Figure 22). All the scaffolds exhibited a high inhibitory area

(Figure 22 B). Furthermore, the SEM analysis revealed that biofilm formation is not observed on scaffolds' surface (Figure 22 A). Such results can be explained by the presence of the CH in all scaffolds' formulations, which is widely described in the literature as a polymer with antibacterial activity [144, 169, 181]. CH can disturb the bacterial growth through the interaction of its positively charged amine groups with the electronegative residues present at bacterial cell wall surface, which increase cell wall permeability and subsequently the leakage of intracellular constituents, leading to dissipation of ionic gradients within the bacteria. Furthermore, CH can also form a barrier on the surface of the bacteria, preventing nutrients from entering into the bacteria [182].

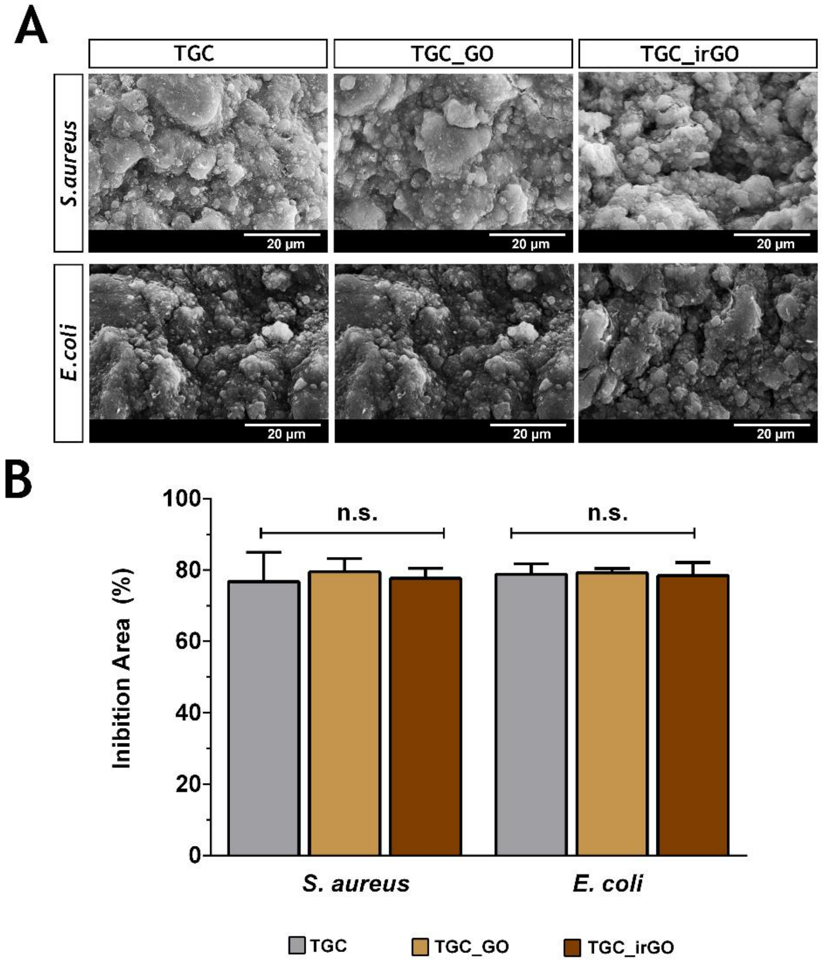

**Figure 22.** Characterization of the antimicrobial activity of the produced scaffolds. SEM images of scaffolds' surface after being in contact with S. aureus and E. coli (A); Analysis of the area of inhibition percentage obtained for scaffolds in contact with S. aureus and E. coli strain (B) (each result is presented in percentage and is the mean ± standard deviation, n = 3; the groups assigned with n.s. were not statistically significant).

# Chapter IV

# 4. Conclusion and Future Perspectives

Researchers from BTE are developing new 3D structures aimed to mimic the bone structure and composition. To accomplish that, researchers have been using composite materials that display the required properties to be used in bone regeneration. Moreover, several techniques have been applied in the scaffolds' production. Among them, RP based techniques have received enormous attention due to its precise control over scaffold architecture, allowing the production of complex, porous and biodegradable structures. In recent studies, scaffolds have been functionalized with graphene-derived materials to improve their mechanical and osteogenic properties. In fact, the rGO possess great compressive strength and higher calcium absorption capability. However, the direct incorporation of rGO into 3D scaffolds is hindered due to its low stability in aqueous solutions.

In present study, TGC printed scaffolds were functionalized with rGO (TGC_irGO), through the LAA-mediated *in situ* reduction of the GO. Such reduction method of GO demonstrated to be an effective process, without interfering with printability of the scaffolds and preserving its initial structure.
Regarding the mechanical performance, the functionalization with rGO into TGC scaffolds revealed increased properties, presenting Cs values (≈ 33 MPa), which are similar to those displayed by the native trabecular bone (2-20 MPa). Further, porosity of TGC_irGO scaffolds did not impair their mechanical properties. Additionally, the biocompatibility profile of scaffolds demonstrated that the functionalization with GO and the rGO did not presented any toxic effect for human osteoblast cells, during 7 days. The surface of scaffolds promotes the cell adhesion whereas the inner structure allows the cell infiltration. Moreover, the scaffolds were able to avoid the microorganism' growth at their surface. Furthermore, TGC_irGO scaffolds were also able to promote the formation of calcium deposition at their surface and were able to augment the alkaline phosphatase activity during 21 days of incubation. Such results highlight the osteoinductive and osteoconductive potential of the scaffolds functionalized with rGO.

Overall, the results reveal the improved potential of TGC_irGO scaffolds for bone repair and also validate the developed *in situ* green reduction protocol.

Hereafter, the *in vivo* performance of the TGC_irGO scaffolds will also be evaluated in order to validate its potential for bone healing applications. Furthermore, complementary assays (e.g. determination of osteopontin, osteocalcin and BMP-2 expression) may be performed to evaluate the osteoinductive and osteoconductive potential of TGC_irGO scaffolds. Moreover, the incorporation of bioactive molecules (growth factors and bone morphogenic proteins) in TGC_irGO scaffolds can be hypothesized in order to further enhance the performance of these scaffolds on bone healing process.

# Chapter V

# 5. References

1. Porter JR, Ruckh TT, Popat KC. Bone tissue engineering: a review in bone biomimetics and drug delivery strategies. Biotechnology progress. 2009; 25(6):1539-60.

2. Amini AR, Laurencin CT, Nukavarapu SP. Bone tissue engineering: recent advances and challenges. Critical Reviews™ in Biomedical Engineering. 2012; 40(5):363-408.

3. Li JJ, Ebied M, Xu J, Zreiqat H. Current Approaches to Bone Tissue Engineering: The Interface between Biology and Engineering. Advanced healthcare materials. 2018; 7(6):1701061.

4. Florencio-Silva R, Sasso GRdS, Sasso-Cerri E, Simões MJ, Cerri PS. Biology of bone tissue: structure, function, and factors that influence bone cells. BioMed Research International. 2015; 2015.

5. Doblaré M, Garcıa J, Gómez M. Modelling bone tissue fracture and healing: a review. Engineering Fracture Mechanics. 2004; 71(13-14):1809-40.

6. Mistry AS, Mikos AG. Tissue engineering strategies for bone regeneration. Regenerative medicine II. Vol. 94: Springer. 2005; 1-22.

7. Peres JA, Lamano T. Strategies for stimulation of new bone formation: a critical review. Brazilian Dental Journal. 2011; 22(6):443-8.

8. Bao CLM, Teo EY, Chong MS, Liu Y, Choolani M, Chan JK. Advances in bone tissue engineering. Regenerative Medicine and Tissue Engineering: InTech. 2013; 600-14.

9. Downey PA, Siegel MI. Bone biology and the clinical implications for osteoporosis. Physical Therapy. 2006; 86(1):77-91.

10. Le BQ, Nurcombe V, Cool SM, van Blitterswijk CA, de Boer J, LaPointe VLS. The Components of Bone and What They Can Teach Us about Regeneration. Materials. 2017; 11(1):14.

11. Boskey AL. Bone composition: relationship to bone fragility and antiosteoporotic drug effects. BoneKEy reports. 2013; 2:447.

12. Clarke B. Normal bone anatomy and physiology. Clinical Journal of the American Society of Nephrology. 2008; 3(3):S131-S9.

13. Sommerfeldt D, Rubin C. Biology of bone and how it orchestrates the form and function of the skeleton. European Spine Journal. 2001; 10(2):S86-S95.

14. Morrison SJ, Scadden DT. The bone marrow niche for haematopoietic stem cells. Nature. 2014; 505(7483):327-34.

15. Ralston SH. Structure and metabolism of bone. Medicine. 2005; 33(12):58-60.

16. www.bloginonline.com/structure-of-the-long-bone/structure-of-the-long-bone-structure-of-long-bones-structure-of-a-typical-long-bone-anatomy-of/ (Accessed in 24/09/2018)

17. Oftadeh R, Perez-Viloria M, Villa-Camacho JC, Vaziri A, Nazarian A. Biomechanics and mechanobiology of trabecular bone: a review. Journal of Biomechanical Engineering. 2015; 137(1):0108021-01080215.

18. Salgado AJ, Coutinho OP, Reis RL. Bone tissue engineering: state of the art and future trends. Macromolecular Bioscience. 2004; 4(8):743-65.

19. Reis RL, San Román J. Biodegradable systems in tissue engineering and regenerative medicine: Crc Press; 2004.

20. Chappard D, Baslé M-F, Legrand E, Audran M. Trabecular bone microarchitecture: a review. Morphologie. 2008; 92(299):162-70.

21. Bandyopadhyay-Ghosh S. Bone as a collagen-hydroxyapatite composite and its repair. Trends in Biomaterials and Artificial Organs. 2008; 22(2):116-24.

22. Shapiro F. Bone development and its relation to fracture repair. The role of mesenchymal osteoblasts and surface osteoblasts. European Cells & Materials. 2008; 15:53-76.

23. Bilezikian JP, Raisz LG, Martin TJ. Principles of bone biology: Academic Press; 2008.

24. Farbod K, Nejadnik MR, Jansen JA, Leeuwenburgh SC. Interactions between inorganic and organic phases in bone tissue as a source of inspiration for design of novel nanocomposites. Tissue Engineering Part B: Reviews. 2013; 20(2):173-88.

25. Chavassieux P, Seeman E, Delmas P. Insights into material and structural basis of bone fragility from diseases associated with fractures: how determinants of the biomechanical properties of bone are compromised by disease. Endocrine Reviews. 2007; 28(2):151-64.

26. Oryan A, Monazzah S, Bigham-Sadegh A. Bone injury and fracture healing biology. Biomedical Environmental Sciences. 2015; 28(1):57-71.

27. Wise ER, Maltsev S, Davies ME, Duer MJ, Jaeger C, Loveridge N, et al. The organic–mineral interface in bone is predominantly polysaccharide. Chemistry of Materials. 2007; 19(21):5055-7.

28. Young MF, Kerr JM, Ibaraki K, Heegaard A-M, Robey PG. Structure, expression, and regulation of the major noncollagenous matrix proteins of bone. Clinical Orthopaedics and Related Research. 1992; (281):275-94.

29. Sroga GE, Vashishth D. Effects of bone matrix proteins on fracture and fragility in osteoporosis. Current Osteoporosis Reports. 2012; 10(2):141-50.

30. Feng B, Jinkang Z, Zhen W, Jianxi L, Jiang C, Jian L, et al. The effect of pore size on tissue ingrowth and neovascularization in porous bioceramics of controlled architecture in vivo. Biomedical Materials. 2011; 6(1):015007.

31. Buck DW, Dumanian GA. Bone biology and physiology: Part II. Clinical correlates. Plastic and Reconstructive Surgery. 2012; 129(6):950e-6e.

32. Bailey AJ, Sims TJ, Ebbesen EN, Mansell JP, Thomsen JS, Mosekilde L. Age-related changes in the biochemical properties of human cancellous bone collagen: relationship to bone strength. Calcified Tissue International. 1999; 65(3):203-10.

33. Jayakumar P, Di Silvio L. Osteoblasts in bone tissue engineering. Proceedings of the Institution of Mechanical Engineers, Part H: Journal of Engineering in Medicine. 2010; 224(12):1415-40.

34. www.york.ac.uk/res/bonefromblood/background/boneremodelling.html (Accessed in 24/09/018)

35. Mackie E. Osteoblasts: novel roles in orchestration of skeletal architecture. The International Journal of Biochemistry & Cell Biology. 2003; 35(9):1301-5.

36. Mellon S, Tanner K. Bone and its adaptation to mechanical loading: a review. International Materials Reviews. 2012; 57(5):235-55.

37. Miller SC, Bowman B, Jee W. Bone lining cells: structure and function. Scanning Microscopy. 1989; 3(3):953-61.

38. Kular J, Tickner J, Chim SM, Xu J. An overview of the regulation of bone remodelling at the cellular level. Clinical Biochemistry. 2012; 45(12):863-73.

39. Delgado-Calle J, Bellido T. Osteocytes and skeletal pathophysiology. Current Molecular Biology Reports. 2015; 1(4):157-67.

40. Civitelli R. Cell–cell communication in the osteoblast/osteocyte lineage. Archives of Biochemistry and Biophysics. 2008; 473(2):188-92.

41. Schaffler MB, Cheung W-Y, Majeska R, Kennedy O. Osteocytes: master orchestrators of bone. Calcified Tissue International. 2014; 94(1):5-24.

42. Bonewald LF. Mechanosensation and transduction in osteocytes. BoneKEy-Osteovision. 2006; 3(10):7-15.

43. Klein-Nulend J, Bakker AD, Bacabac RG, Vatsa A, Weinbaum S. Mechanosensation and transduction in osteocytes. Bone. 2013; 54(2):182-90.

44. Dudley HR, Spiro D. The fine structure of bone cells. The Journal of Cell Biology. 1961; 11(3):627-49.

45. Cohen Jr MM. The new bone biology: pathologic, molecular, and clinical correlates. American Journal of Medical Genetics Part A. 2006; 140(23):2646-706.

46. Henkel J, Woodruff MA, Epari DR, Steck R, Glatt V, Dickinson IC, et al. Bone regeneration based on tissue engineering conceptions—a 21st century perspective. Bone Research. 2013; 1(3):216-48.

47. Einhorn TA, Gerstenfeld LC. Fracture healing: mechanisms and interventions. Nature Reviews Rheumatology. 2015; 11(1):45-54.

48. Wang W, Yeung KW. Bone grafts and biomaterials substitutes for bone defect repair: A review. Bioactive Materials. 2017; 2(4):224-47.

49. Marsell R, Einhorn TA. The biology of fracture healing. Injury. 2011; 42(6):551-5.

50. Clarkin C, Olsen BR. On bone-forming cells and blood vessels in bone development. Cell Metabolism. 2010; 12(4):314-6.

51. Wang X, Wang Y, Gou W, Lu Q, Peng J, Lu S. Role of mesenchymal stem cells in bone regeneration and fracture repair: a review. International Orthopaedics. 2013; 37(12):2491-8.

52. Knight MN, Hankenson KD. Mesenchymal stem cells in bone regeneration. Advances in Wound Care. 2013; 2(6):306-16.

53. Gerstenfeld LC, Alkhiary YM, Krall EA, Nicholls FH, Stapleton SN, Fitch JL, et al. Three-dimensional reconstruction of fracture callus morphogenesis. Journal of Histochemistry & Cytochemistry. 2006; 54(11):1215-28.

54. Ai-Aql Z, Alagl AS, Graves DT, Gerstenfeld LC, Einhorn TA. Molecular mechanisms controlling bone formation during fracture healing and distraction osteogenesis. Journal of Dental Research. 2008; 87(2):107-18.

55. Boonrungsiman S, Gentleman E, Carzaniga R, Evans ND, McComb DW, Porter AE, et al. The role of intracellular calcium phosphate in osteoblast-mediated bone apatite formation. Proceedings of the National Academy of Sciences. 2012; 109(35):14170-5.

56. Ghiasi MS, Chen J, Vaziri A, Rodriguez EK, Nazarian A. Bone fracture healing in mechanobiological modeling: A review of principles and methods. Bone Reports. 2017; 6:87-100.

57. Pillion JP, Vernick D, Shapiro J. Hearing loss in osteogenesis imperfecta: characteristics and treatment considerations. Genetics Research International. 2011; 2011.

58. Ginaldi L, Di Benedetto MC, De Martinis M. Osteoporosis, inflammation and ageing. Immunity & Ageing. 2005; 2(1):14.

59. Lew DP, Waldvogel FA. Osteomyelitis. The Lancet. 2004; 364(9431):369-79.

60. Lavrador P, Gaspar VM, Mano JF. Stimuli-responsive nanocarriers for delivery of bone therapeutics-Barriers and progresses. Journal of Controlled Release. 2018; 273:51-67.

61. Sözen T, Özışık L, Başaran NÇ. An overview and management of osteoporosis. European Journal of Rheumatology. 2017; 4(1):46-56.

62. Whyte MP. Paget's disease of bone. New England Journal of Medicine. 2006; 355(6):593-600.

63. Ferraz-de-Souza B, Correa PHS. Diagnosis and treatment of Paget's disease of bone: a mini-review. Arquivos Brasileiros de Endocrinologia & Metabologia. 2013; 57(8):577-82.

64. Feng X, McDonald JM. Disorders of bone remodeling. Annual Review of Pathology: Mechanisms of Disease. 2011; 6:121-45.

65. Shapiro F. Bone and Joint Deformity in Metabolic, Inflammatory, Neoplastic, Infectious, and Hematologic Disorders. Pediatric Orthopedic Deformities. Vol. 1: Springer. 2016; 411-504.

66. Chen D, Shen J, Zhao W, Wang T, Han L, Hamilton JL, et al. Osteoarthritis: toward a comprehensive understanding of pathological mechanism. Bone Research. 2017; 5:16044.

67. Loeser RF, Goldring SR, Scanzello CR, Goldring MB. Osteoarthritis: a disease of the joint as an organ. Arthritis & Rheumatism. 2012; 64(6):1697-707.

68. Frohlich M, Grayson WL, Wan LQ, Marolt D, Drobnic M, Vunjak-Novakovic G. Tissue engineered bone grafts: biological requirements, tissue culture and clinical relevance. Current Stem Cell Research & Therapy. 2008; 3(4):254-64.

69. Nazirkar G, Singh S, Dole V, Nikam A. Effortless effort in bone regeneration: a review. Journal of International Oral Health: JIOH. 2014; 6(3):120-4.

70. Howard D, Buttery LD, Shakesheff KM, Roberts SJ. Tissue engineering: strategies, stem cells and scaffolds. Journal of Anatomy. 2008; 213(1):66-72.

71. Bose S, Roy M, Bandyopadhyay A. Recent advances in bone tissue engineering scaffolds. Trends in Biotechnology. 2012; 30(10):546-54.

72. Costa JB, Pereira H, Espregueira-Mendes J, Khang G, Oliveira JM, Reis RL. Tissue engineering in orthopaedic sports medicine: current concepts. Journal of ISAKOS: Joint Disorders & Orthopaedic Sports Medicine. 2017; 2(2):60-6.

73. O'brien FJ. Biomaterials & scaffolds for tissue engineering. Materials Today. 2011; 14(3):88-95.

74. Mitra J, Tripathi G, Sharma A, Basu B. Scaffolds for bone tissue engineering: role of surface patterning on osteoblast response. RSC Advances. 2013; 3(28):11073-94.

75. Dhandayuthapani B, Yoshida Y, Maekawa T, Kumar DS. Polymeric scaffolds in tissue engineering application: a review. International Journal of Polymer Science. 2011; 2011.

76. Bružauskaitė I, Bironaitė D, Bagdonas E, Bernotienė E. Scaffolds and cells for tissue regeneration: different scaffold pore sizes—different cell effects. Cytotechnology. 2016; 68(3):355-69.

77. Polo-Corrales L, Latorre-Esteves M, Ramirez-Vick JE. Scaffold design for bone regeneration. Journal of Nanoscience and Nanotechnology. 2014; 14(1):15-56.

78. Karageorgiou V, Kaplan D. Porosity of 3D biomaterial scaffolds and osteogenesis. Biomaterials. 2005; 26(27):5474-91.

79. Campoccia D, Montanaro L, Arciola CR. A review of the clinical implications of anti-infective biomaterials and infection-resistant surfaces. Biomaterials. 2013; 34(33):8018-29.

80. Fux CA, Stoodley P, Hall-Stoodley L, Costerton JW. Bacterial biofilms: a diagnostic and therapeutic challenge. Expert Review of Anti-Infective Therapy. 2003; 1(4):667-83.

81. Khosravi A, Ahmadi F, Salmanzadeh S, Dashtbozorg A, Montazeri EA. Study of bacteria isolated from orthopedic implant infections and their antimicrobial susceptibility pattern. Research Journal of Microbiology. 2009; 4(4):158-63.

82. Crémet L, Broquet A, Brulin B, Jacqueline C, Dauvergne S, Brion R, et al. Pathogenic potential of Escherichia coli clinical strains from orthopedic implant infections towards human osteoblastic cells. Pathogens and Disease. 2015; 73(8).

83. Álvarez-Paino M, Muñoz-Bonilla A, Fernández-García M. Antimicrobial polymers in the nano-world. Nanomaterials. 2017; 7(2):48.

84. Yuan B, Zhou S-y, Chen X-s. Rapid prototyping technology and its application in bone tissue engineering. Journal of Zhejiang University-Science B. 2017; 18(4):303-15.

85. Salerno A, Oliviero M, Di Maio E, Iannace S, Netti P. Design of porous polymeric scaffolds by gas foaming of heterogeneous blends. Journal of Materials Science: Materials in Medicine. 2009; 20(10):2043-51.

86. Lv Q, Feng Q. Preparation of 3-D regenerated fibroin scaffolds with freeze drying method and freeze drying/foaming technique. Journal of Materials Science: Materials in Medicine. 2006; 17(12):1349-56.

87. Munir N, Callanan A. Novel phase separated PCL/collagen scaffolds for cartilage tissue engineering. Biomedical Materials. 2018; 13(5).

88. Park HJ, Lee OJ, Lee MC, Moon BM, Ju HW, min Lee J, et al. Fabrication of 3D porous silk scaffolds by particulate (salt/sucrose) leaching for bone tissue reconstruction. International Journal of Biological Macromolecules. 2015; 78:215-23.

89. Loh QL, Choong C. Three-dimensional scaffolds for tissue engineering applications: role of porosity and pore size. Tissue Engineering Part B: Reviews. 2013; 19(6):485-502.

90. Malda J, Visser J, Melchels FP, Jüngst T, Hennink WE, Dhert WJ, et al. 25th anniversary article: engineering hydrogels for biofabrication. Advanced materials. 2013; 25(36):5011-28.

91. Malone E, Lipson H. Fab@ Home: the personal desktop fabricator kit. Rapid Prototyping Journal. 2007; 13(4):245-55.

92. Cohen DL, Lipton JI, Bonassar LJ, Lipson H. Additive manufacturing for in situ repair of osteochondral defects. Biofabrication. 2010; 2(3):035004.

93. Diogo GS, Gaspar VM, Serra IR, Fradique R, Correia IJ. Manufacture of β-TCP/alginate scaffolds through a Fab@home model for application in bone tissue engineering. Biofabrication. 2014; 6(2):025001.

94. Do AV, Khorsand B, Geary SM, Salem AK. 3D printing of scaffolds for tissue regeneration applications. Advanced healthcare materials. 2015; 4(12):1742-62.

95. Fradique R, Correia TR, Miguel S, De Sa K, Figueira D, Mendonça A, et al. Production of new 3D scaffolds for bone tissue regeneration by rapid prototyping. Journal of Materials Science: Materials in Medicine. 2016; 27(4):69.

96. Kang K, Hockaday L, Butcher J. Quantitative optimization of solid freeform deposition of aqueous hydrogels. Biofabrication. 2013; 5(3):035001.

97. Bose S, Vahabzadeh S, Bandyopadhyay A. Bone tissue engineering using 3D printing. Materials Today. 2013; 16(12):496-504.

98. Kheirallah M, Almeshaly H. Bone graft substitutes for bone defect regeneration. A collective review. International Journal of Dentistry and Oral Science. 2016; 3(5):247-57.

99. Wen Y, Xun S, Haoye M, Baichuan S, Peng C, Xuejian L, et al. 3D printed porous ceramic scaffolds for bone tissue engineering: a review. Biomaterials Science. 2017; 5(9):1690-8.

100. Wongwitwichot P, Kaewsrichan J, Chua K, Ruszymah B. Comparison of TCP and TCP/HA hybrid scaffolds for osteoconductive activity. The Open Biomedical Engineering Journal. 2010; 4:279-85.

101. Seol Y-J, Park JY, Jung JW, Jang J, Girdhari R, Kim SW, et al. Improvement of bone regeneration capability of ceramic scaffolds by accelerated release of their calcium ions. Tissue Engineering Part A. 2014; 20(21-22):2840-9.

102. Santos CF, Silva AP, Lopes L, Pires I, Correia IJ. Design and production of sintered β-tricalcium phosphate 3D scaffolds for bone tissue regeneration. Materials Science and Engineering: C. 2012; 32(5):1293-8.

103. Huang B, Caetano G, Vyas C, Blaker JJ, Diver C, Bártolo P. Polymer-ceramic composite scaffolds: The effect of hydroxyapatite and β-tri-calcium phosphate. Materials. 2018; 11(1):129.

104. Vroman I, Tighzert L. Biodegradable polymers. Materials. 2009; 2(2):307-44.

105. Liu Q, Li Q, Xu S, Zheng Q, Cao X. Preparation and Properties of 3D Printed Alginate-Chitosan Polyion Complex Hydrogels for Tissue Engineering. Polymers. 2018; 10(6):664.

106. Schieker M, Seitz H, Drosse I, Seitz S, Mutschler W. Biomaterials as scaffold for bone tissue engineering. European Journal of Trauma. 2006; 32(2):114-24.

107. Kroeze R, Helder M, Govaert L, Smit T. Biodegradable polymers in bone tissue engineering. Materials. 2009; 2(3):833-56.

108. Gómez-Guillén M, Giménez B, López-Caballero Ma, Montero M. Functional and bioactive properties of collagen and gelatin from alternative sources: A review. Food Hydrocolloids. 2011; 25(8):1813-27.

109. Hoque ME, Nuge T, Yeow TK, Nordin N, Prasad R. Gelatin based scaffolds for tissue engineering-a review. Polymers Research Journal. 2015; 9(1):15-32.

110. Rose JB, Pacelli S, Haj AJE, Dua HS, Hopkinson A, White LJ, et al. Gelatin-based materials in ocular tissue engineering. Materials. 2014; 7(4):3106-35.

111. Zhao W, Jin X, Cong Y, Liu Y, Fu J. Degradable natural polymer hydrogels for articular cartilage tissue engineering. Journal of Chemical Technology & Biotechnology. 2013; 88(3):327-39.

112. Stratton S, Shelke NB, Hoshino K, Rudraiah S, Kumbar SG. Bioactive polymeric scaffolds for tissue engineering. Bioactive Materials. 2016; 1(2):93-108.

113. Venkatesan J, Kim S-K. Chitosan composites for bone tissue engineering—an overview. Marine Drugs. 2010; 8(8):2252-66.

114. Rodríguez-Vázquez M, Vega-Ruiz B, Ramos-Zúñiga R, Saldaña-Koppel DA, Quiñones-Olvera LF. Chitosan and its potential use as a scaffold for tissue engineering in regenerative medicine. BioMed Research International. 2015; 2015.

115. Croisier F, Jérôme C. Chitosan-based biomaterials for tissue engineering. European Polymer Journal. 2013; 49(4):780-92.

116. Lončarević A, Ivanković M, Rogina A. Lysozyme-induced Degradation of Chitosan: the Characterisation of Degraded Chitosan Scaffolds. Journal of Tissue Repair and Regeneration. 2017; 1(1):12-22.

117. Prakasam M, Locs J, Salma-Ancane K, Loca D, Largeteau A, Berzina-Cimdina L. Biodegradable materials and metallic implants—a review. Journal of Functional Biomaterials. 2017; 8(4):44.

118. Turnbull G, Clarke J, Picard F, Riches P, Jia L, Han F, et al. 3D bioactive composite scaffolds for bone tissue engineering. Bioactive Materials. 2018; 3(3):278-314.

119. Chiara G, Letizia F, Lorenzo F, Edoardo S, Diego S, Stefano S, et al. Nanostructured biomaterials for tissue engineered bone tissue reconstruction. International Journal of Molecular Sciences. 2012; 13(1):737-57.

120. Cheng C, Li S, Thomas A, Kotov NA, Haag R. Functional graphene nanomaterials based architectures: biointeractions, fabrications, and emerging biological applications. Chemical Reviews. 2017; 117(3):1826-914.

121. Boga JC, Miguel SP, de Melo-Diogo D, Mendonça AG, Louro RO, Correia IJ. In vitro characterization of 3D printed scaffolds aimed at bone tissue regeneration. Colloids and Surfaces B: Biointerfaces. 2018; 165:207-18.

122. de Melo-Diogo D, Pais-Silva C, Costa EC, Louro RO, Correia IJ. D-α-tocopheryl polyethylene glycol 1000 succinate functionalized nanographene oxide for cancer therapy. Nanomedicine. 2017; 12(5):443-56.

123. Skákalová V, Kotrusz P, Jergel M, Susi T, Mittelberger A, Vretenár V, et al. Chemical Oxidation of Graphite: Evolution of the Structure and Properties. The Journal of Physical Chemistry C. 2017; 122(1):929-35.

124. Kumar V, Kumar A, Bhandari S, Biradar A, Reddy G, Pasricha R. Exfoliation of graphene oxide and its application in improving the electro-optical response of ferroelectric liquid crystal. Journal of Applied Physics. 2015; 118(11):114904.

125. Perrozzi F, Prezioso S, Ottaviano L. Graphene oxide: from fundamentals to applications. Journal of Physics: Condensed Matter. 2014; 27(1):013002.

126. Li F, Jiang X, Zhao J, Zhang S. Graphene oxide: A promising nanomaterial for energy and environmental applications. Nano Energy. 2015; 16:488-515.

127. Nair M, Nancy D, Krishnan AG, Anjusree G, Vadukumpully S, Nair SV. Graphene oxide nanoflakes incorporated gelatin–hydroxyapatite scaffolds enhance osteogenic differentiation of human mesenchymal stem cells. Nanotechnology. 2015; 26(16):161001.

128. Liu H, Cheng J, Chen F, Bai D, Shao C, Wang J, et al. Gelatin functionalized graphene oxide for mineralization of hydroxyapatite: biomimetic and in vitro evaluation. Nanoscale. 2014; 6(10):5315-22.

129. Holt BD, Arnold AM, Sydlik SA. In it for the long haul: the cytocompatibility of aged graphene oxide and its degradation products. Advanced Healthcare Materials. 2016; 5(23):3056-66.

130. Sanchez VC, Jachak A, Hurt RH, Kane AB. Biological interactions of graphene-family nanomaterials: an interdisciplinary review. Chemical Research in Toxicology. 2011; 25(1):15-34.

131. Pei S, Cheng H-M. The reduction of graphene oxide. Carbon. 2012; 50(9):3210-28.

132. Kanayama I, Miyaji H, Takita H, Nishida E, Tsuji M, Fugetsu B, et al. Comparative study of bioactivity of collagen scaffolds coated with graphene oxide and reduced graphene oxide. International Journal of Nanomedicine. 2014; 9:3363-73.

133. Stankovich S, Dikin DA, Piner RD, Kohlhaas KA, Kleinhammes A, Jia Y, et al. Synthesis of graphene-based nanosheets via chemical reduction of exfoliated graphite oxide. Carbon. 2007; 45(7):1558-65.

134. Chua CK, Pumera M. The reduction of graphene oxide with hydrazine: elucidating its reductive capability based on a reaction-model approach. Chemical Communications. 2016; 52(1):72-5.

135. De Silva KKH, Huang H-H, Yoshimura M. Progress of reduction of graphene oxide by ascorbic acid. Applied Surface Science. 2018; 447:338-46.

136. Chowdhury I, Mansukhani ND, Guiney LM, Hersam MC, Bouchard D. Aggregation and stability of reduced graphene oxide: complex roles of divalent cations, pH, and natural organic matter. Environmental Science & Technology. 2015; 49(18):10886-93.

137. Park CM, Wang D, Heo J, Her N, Su C. Aggregation of reduced graphene oxide and its nanohybrids with magnetite and elemental silver under environmentally relevant conditions. Journal of Nanoparticle Research. 2018; 20(4):93.

138. Kim J-W, Shin YC, Lee J-J, Bae E-B, Jeon Y-C, Jeong C-M, et al. The effect of reduced graphene oxide-coated biphasic calcium phosphate bone graft material on osteogenesis. International Journal of Molecular Sciences. 2017; 18(8):1725.

139. Correia TR, Figueira DR, de Sá KD, Miguel SP, Fradique RG, Mendonça AG, et al. 3D Printed scaffolds with bactericidal activity aimed for bone tissue regeneration. International Journal of Biological Macromolecules. 2016; 93(Part B):1432-45.

140. Kokubo T, Takadama H. How useful is SBF in predicting in vivo bone bioactivity? Biomaterials. 2006; 27(15):2907-15.

141. Torres AL, Gaspar VM, Serra IR, Diogo GS, Fradique R, Silva AP, et al. Bioactive polymeric–ceramic hybrid 3D scaffold for application in bone tissue regeneration. Materials Science and Engineering: C. 2013; 33(7):4460-9.

142. Valente J, Valente TAM, Alves P, Ferreira P, Silva A, Correia I. Alginate based scaffolds for bone tissue engineering. Materials Science and Engineering: C. 2012; 32(8):2596-603.

143. Jiankang H, Dichen L, Yaxiong L, Bo Y, Bingheng L, Qin L. Fabrication and characterization of chitosan/gelatin porous scaffolds with predefined internal microstructures. Polymer. 2007; 48(15):4578-88.

144. Miguel PS, Ribeiro PM, Coutinho P, Correia JI. Electrospun Polycaprolactone/Aloe Vera_Chitosan Nanofibrous Asymmetric Membranes Aimed for Wound Healing Applications. Polymers. 2017; 9(5):183.

145. Moreau JL, Xu HHK. Mesenchymal stem cell proliferation and differentiation on an injectable calcium phosphate-chitosan composite scaffold. Biomaterials. 2009; 30(14):2675-82.

146. Choi D, Kumta PN. Mechano-chemical synthesis and characterization of nanostructured β-TCP powder. Materials Science and Engineering: C. 2007; 27(3):377-81.

147. Yang K, Wan J, Zhang S, Tian B, Zhang Y, Liu Z. The influence of surface chemistry and size of nanoscale graphene oxide on photothermal therapy of cancer using ultra-low laser power. Biomaterials. 2012; 33(7):2206-14.

148. Lima-Sousa R, de Melo-Diogo D, Alves CG, Costa EC, Ferreira P, Louro RO, et al. Hyaluronic acid functionalized green reduced graphene oxide for targeted cancer photothermal therapy. Carbohydrate Polymers. 2018; 200:93-9.

149. Alava T, Mann JA, Théodore Cc, Benitez JJ, Dichtel WR, Parpia JM, et al. Control of the graphene-protein interface is required to preserve adsorbed protein function. Analytical Chemistry. 2013; 85(5):2754-9.

150. Park JS, Goo N-I, Kim D-E. Mechanism of DNA adsorption and desorption on graphene oxide. Langmuir. 2014; 30(42):12587-95.

151. Burg KJ, Porter S, Kellam JF. Biomaterial developments for bone tissue engineering. Biomaterials. 2000; 21(23):2347-59.

152. Miranda SC, Silva GA, Hell RC, Martins MD, Alves JB, Goes AM. Three-dimensional culture of rat BMMSCs in a porous chitosan-gelatin scaffold: A promising association for bone tissue engineering in oral reconstruction. Archives of Oral Biology. 2011; 56(1):1-15.

153. Bi L, Cheng W, Fan H, Pei G. Reconstruction of goat tibial defects using an injectable tricalcium phosphate/chitosan in combination with autologous platelet-rich plasma. Biomaterials. 2010; 31(12):3201-11.

154. Tao L, Zhonglong L, Ming X, Zezheng Y, Zhiyuan L, Xiaojun Z, et al. In vitro and in vivo studies of a gelatin/carboxymethyl chitosan/LAPONITE® composite scaffold for bone tissue engineering. RSC Advances. 2017; 7(85):54100-10.

155. Thein-Han W, Misra R. Biomimetic chitosan-nanohydroxyapatite composite scaffolds for bone tissue engineering. Acta Biomaterialia. 2009; 5(4):1182-97.

156. De Sá KD, Figueira DR, Miguel SP, Correia TR, Silva AP, Correia IJ. 3D scaffolds coated with nanofibers displaying bactericidal activity for bone tissue applications. International Journal of Polymeric Materials and Polymeric Biomaterials. 2017; 66(9):432-42.

157. Wei J, Igarashi T, Okumori N, Igarashi T, Maetani T, Liu B, et al. Influence of surface wettability on competitive protein adsorption and initial attachment of osteoblasts. Biomedical Materials. 2009; 4(4):045002.

158. Guo S, Zhu X, Li M, Shi L, Ong JLT, Jańczewski D, et al. Parallel control over surface charge and wettability using polyelectrolyte architecture: effect on protein adsorption and cell adhesion. ACS Applied Materials & Interfaces. 2016; 8(44):30552-63.

159. Oliveira SM, Alves NM, Mano JF. Cell interactions with superhydrophilic and superhydrophobic surfaces. Journal of Adhesion Science and Technology. 2014; 28(8-9):843-63.

160. Dowling DP, Miller IS, Ardhaoui M, Gallagher WM. Effect of surface wettability and topography on the adhesion of osteosarcoma cells on plasma-modified polystyrene. Journal of Biomaterials Applications. 2011; 26(3):327-47.

161. Bacakova L, Filova E, Parizek M, Ruml T, Svorcik V. Modulation of cell adhesion, proliferation and differentiation on materials designed for body implants. Biotechnology advances. 2011; 29(6):739-67.

162. Hollister SJ. Porous scaffold design for tissue engineering. Nature Materials. 2005; 4(7):518-24.

163. Torres-Sanchez C, Al Mushref F, Norrito M, Yendall K, Liu Y, Conway PP. The effect of pore size and porosity on mechanical properties and biological response of porous titanium scaffolds. Materials Science and Engineering: C. 2017; 77:219-28.

164. Ramay HR, Zhang M. Preparation of porous hydroxyapatite scaffolds by combination of the gel-casting and polymer sponge methods. Biomaterials. 2003; 24(19):3293-302.

165. Xiao X, Wang W, Liu D, Zhang H, Gao P, Geng L, et al. The promotion of angiogenesis induced by three-dimensional porous beta-tricalcium phosphate scaffold with different interconnection sizes via activation of PI3K/Akt pathways. Scientific Reports. 2015; 5:9409.

166. Peter M, Ganesh N, Selvamurugan N, Nair S, Furuike T, Tamura H, et al. Preparation and characterization of chitosan-gelatin/nanohydroxyapatite composite scaffolds for tissue engineering applications. Carbohydrate Polymers. 2010; 80(3):687-94.

167. Blair HC, Larrouture QC, Li Y, Lin H, Beer-Stoltz D, Liu L, et al. Osteoblast differentiation and bone matrix formation in vivo and in vitro. Tissue Engineering Part B: Reviews. 2017; 23(3):268-80.

168. Zhou Y, Yao H, Wang J, Wang D, Liu Q, Li Z. Greener synthesis of electrospun collagen/hydroxyapatite composite fibers with an excellent microstructure for bone tissue engineering. International Journal of Nanomedicine. 2015; 10:3203.

169. Serra I, Fradique R, Vallejo M, Correia T, Miguel S, Correia I. Production and characterization of chitosan/gelatin/β-TCP scaffolds for improved bone tissue regeneration. Materials Science and Engineering: C. 2015; 55:592-604.

170. de Melo-Diogo D, Lima-Sousa R, Alves CG, Costa EC, Louro RO, Correia IJ. Functionalization of graphene family nanomaterials for application in cancer therapy. Colloids and Surfaces B: Biointerfaces. 2018; 171:260-75.

171. Davidenko N, Schuster CF, Bax DV, Farndale RW, Hamaia S, Best SM, et al. Evaluation of cell binding to collagen and gelatin: a study of the effect of 2D and 3D architecture and surface chemistry. Journal of Materials Science: Materials in Medicine. 2016; 27(10):148.

172. Liao S, Cui F, Zhu Y. Osteoblasts adherence and migration through three-dimensional porous mineralized collagen based composite: nHAC/PLA. Journal of Bioactive and Compatible Polymers. 2004; 19(2):117-30.

173. Vashisth P, Bellare JR. Development of hybrid scaffold with biomimetic 3D architecture for bone regeneration. Nanomedicine: Nanotechnology, Biology and Medicine. 2018; 14(4):1325-36.

174. Mehrali M, Moghaddam E, Shirazi SFS, Baradaran S, Mehrali M, Latibari ST, et al. Synthesis, mechanical properties, and in vitro biocompatibility with osteoblasts of calcium silicate–reduced graphene oxide composites. ACS Applied Materials & Interfaces. 2014; 6(6):3947-62.

175. Lee JH, Shin YC, Lee S-M, Jin OS, Kang SH, Hong SW, et al. Enhanced osteogenesis by reduced graphene oxide/hydroxyapatite nanocomposites. Scientific Reports. 2015; 5:18833.

176. Marrella A, Tedeschi G, Giannoni P, Lagazzo A, Sbrana F, Barberis F, et al. “Green-reduced” graphene oxide induces in vitro an enhanced biomimetic mineralization of polycaprolactone electrospun meshes. Materials Science and Engineering: C. 2018; 93:1044-53.

177. Zhang X, Chang W, Lee P, Wang Y, Yang M, Li J, et al. Polymer-ceramic spiral structured scaffolds for bone tissue engineering: effect of hydroxyapatite composition on human fetal osteoblasts. PloS One. 2014; 9(1):e85871.

178. Lee JB, Kim JE, Bae MS, Park SA, Balikov DA, Sung H-j, et al. Development of Poly (ε-caprolactone) Scaffold Loaded with Simvastatin and Beta-Cyclodextrin Modified Hydroxyapatite Inclusion Complex for Bone Tissue Engineering. Polymers. 2016; 8(2):49.

179. Maeno S, Niki Y, Matsumoto H, Morioka H, Yatabe T, Funayama A, et al. The effect of calcium ion concentration on osteoblast viability, proliferation and differentiation in monolayer and 3D culture. Biomaterials. 2005; 26(23):4847-55.

180. Channasanon S, Udomkusonsri P, Chantaweroad S, Tesavibul P, Tanodekaew S. Gentamicin Released from Porous Scaffolds Fabricated by Stereolithography. Journal of healthcare engineering. 2017; 2017.

181. Miguel SP, Ribeiro MP, Brancal H, Coutinho P, Correia IJ. Thermoresponsive chitosan-agarose hydrogel for skin regeneration. Carbohydrate Polymers. 2014; 111:366-73.

182. Simões D, Miguel SP, Ribeiro MP, Coutinho P, Mendonça AG, Correia IJ. Recent advances on antimicrobial wound dressing: a review. European Journal of Pharmaceutics and Biopharmaceutics. 2018; 127:130-41.